RMetS
Royal Meteorological Society

Intraseasonal variability of tropical Atlantic sea-surface temperature: air–sea interaction over upwelling fronts

Moussa Diakhaté,[a,b]* Gaëlle de Coëtlogon,[c] Alban Lazar,[b] Malick Wade[a] and Amadou T. Gaye[a]

[a]*Laboratoire de Physique de l'Atmosphère et de l'Océan – Siméon Fongang (LPAO-SF), Dakar, Senegal*
[b]*Laboratoire d'Océanographie et Climat, Expérimentations et Approches Numériques (LOCEAN), Paris, France*
[c]*Laboratoire Atmosphère, Milieux, et Observations Spatiales (LATMOS), Paris, France*

*Correspondence to: M. Diakhaté, Laboratoire de Physique de l'Atmosphère et de l'Océan – Siméon Fongang (LPAO-SF), 10700 Dakar, BP 5085, Senegal. E-mail: moussa1.diakhate@ucad.edu.sn; moussa.diakhate@locean-ipsl.upmc.fr

Tropical Atlantic sea-surface temperatures (SSTs) maximum intraseasonal variability (ISV) and their interaction with local surface winds are investigated, applying statistical analysis to observations and to a recent coupled reanalysis over the 2000–2009 decade. Five cores of strong ISV emerge, with standard deviation reaching about 1 °C in frontal areas of the three main upwelling systems: equatorial, Angola-Benguela and Senegal-Mauritania (the southern side of the Canary upwelling). West of 10 °W along the Equator, a 20–60-day peak caused by tropical instability waves is shown to generate surface wind anomalies through the adjustment of the horizontal surface pressure gradient in addition to the modification of near-surface atmospheric stratification. East of 10°W along the Equator, an intense biweekly oscillation increases the ocean and atmosphere ISV. In the two coastal upwelling fronts, intraseasonal SST anomalies resemble each other. They are shown to be influenced by coastal Kelvin waves in addition to large-scale wind forcing. Over the Angola-Benguela upwelling, coastal wind bursts controlling the SST ISV are associated with anomalously strong pressure patterns related to the Madden–Julian Oscillation, the St Helena anticyclone and the Antarctic Oscillation. In the Senegal-Mauritania upwelling, the wind anomalies mainly linked to the Azores anticyclone in the southern front during November to May appear to be connected to the Saharan heat-low in the northern front from June to September. In all five regions and as expected for such upwelling regimes, vertical oceanic mixing represents the dominant term in the mixed-layer heat budget. In the equatorial band, as found in previous studies, horizontal advection is equally important, while it appears surprisingly weak in coastal fronts. Finally, a striking result is the general lack of surface wind signal related to the SST ISV in the coastal upwellings.

Key Words: tropical Atlantic; intraseasonal variability; air–sea interaction

Received 26 September 2014; Revised 26 July 2015; Accepted 11 August 2015; Published online in Wiley Online Library

1. Introduction

The influence of sea-surface temperatures (SSTs) on the low-level atmospheric circulation has become evident in observations only over the past decade, from satellite measurements of SST and surface winds. Before the advent of satellites, analyses of coarse-resolution ship observations in conjunction with coupled climate modeling on similarly coarse scales have generally found a negative correlation between SST and wind speed (Xie, 2004, and references therein). This negative correlation at large scale has been interpreted as the ocean passively responding to wind-induced latent and sensible heat fluxes (i.e. a one-way forcing of the ocean by the atmosphere). However, SST and wind from satellite products reveal that in regions of strong oceanic fronts and eddy activity, such as the Agulhas Return Current, the Gulf Stream region and the Pacific or Atlantic equatorial upwelling regions, surface wind speed is stronger locally over warm waters and weaker over cold waters. This positive correlation signature is interpreted as SST forcing local atmospheric circulation (Small *et al.*, 2008).

Two complementary mechanisms for this oceanic influence on surface winds have been identified. First, cooler SSTs tend to stabilize the atmospheric column and decrease the vertical momentum flux, and decelerate the surface winds. Conversely, warmer SSTs increase the turbulent mixing in the marine atmospheric boundary layer, which increases surface winds (Sweet *et al.*, 1981; Hayes *et al.*, 1989; Wallace *et al.*, 1989; Xie, 2004). Because of this mechanism (hereafter referred to as 'SW', from Sweet *et al.* (1981)), regions with very sharp SST fronts are very sensitive to the coupling between SST and surface winds (Xie, 2004; Small *et al.*, 2008). Second, as the air temperature and moisture respond to surface fluxes, the atmospheric pressure changes (Lindzen and Nigam, 1987). This leads to a spatial

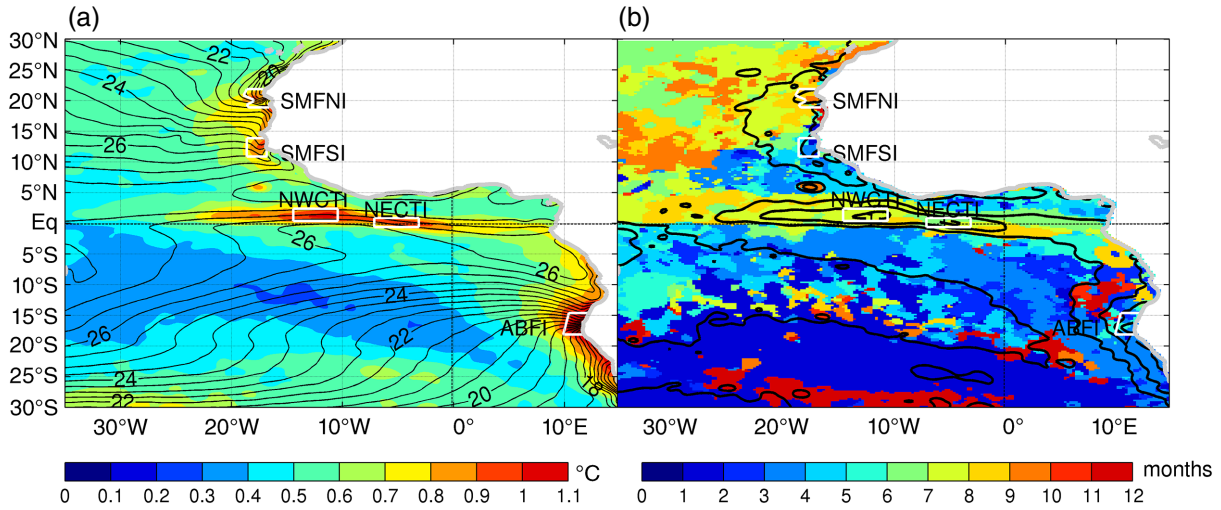

Figure 1. (a) Maximum of the monthly-averaged climatological root-mean-square (r.m.s.) of daily SST anomaly (<90-day filtered, 2000–2009, shading, in °C) and annual mean SST (black contours, in °C). (b) Month (shading) and maximum value (black contours, in °C, same as shading in (a)) of the monthly-averaged climatological r.m.s. of SST anomaly. White boxes represent index areas.

pressure gradient which can drive secondary circulations (Wai and Stage, 1989). This mechanism will be hereafter referred to as 'LN' (from Lindzen and Nigam (1987)).

In the SW mechanism, the response to SST changes in the atmospheric mixed layer is immediate (i.e. within a few hours in the first 100–200 m), while in the LN mechanism it takes 1 or 2 days for the entire atmospheric boundary layer (600–2000 m) to adjust (Leduc-Leballeur *et al.*, 2013; de Coëtlogon *et al.*, 2014).

SST variability in the tropical Atlantic is primarily governed by the seasonal evolution of winds (Xie and Carton, 2004). At the Equator, this seasonal cycle is characterized by the development of a cold tongue during boreal summer (e.g. Caniaux *et al.*, 2011). Although the semi-annual cycle of surface winds is much weaker than their annual cycle, it is considered as the dominant explanation for variations of sea-surface height (SSH) and zonal currents in the cold tongue from March to August according to a numerical study by Ding *et al.* (2009). Using observed data, Foltz *et al.* (2013) reveal that between May and July, as well as in November, the equatorial seasonal cycle of oceanic mixed-layer heat content is balanced by a semi-annual cycle of strong turbulent mixing that cools the mixed layer. An intense meridional SST front therefore appears between the colder upwelling and the warmer off-equatorial waters in the central and eastern basin (Flament *et al.*, 1996; Kennan and Flament, 2000), within which occur prominent intraseasonal fluctuations that are visible from satellite imageries and historical observations (e.g. Chelton *et al.*, 2001; Chelton and Xie, 2010). Similar features are also observed along West Africa and Angola-Benguela coasts during boreal summer and winter respectively (Chelton *et al.*, 2004): the seasonal surface winds induce coastal upwellings and intense SST fronts with strong intraseasonal fluctuations (Figure 1).

However, ocean and atmosphere interaction at the intraseasonal time-scale remains still less documented over the tropical Atlantic compared to the tropical Pacific and off-tropical regions of strong eddy activity (see the reviews by Small *et al.* (2008); or Chelton and Xie (2010)). This is particularly surprising considering that all climate models exhibit strong and systematic SST biases in the eastern tropical Atlantic (e.g. Davey *et al.*, 2002; Richter *et al.*, 2014) that develop within a few weeks (Huang *et al.*, 2007), involving the interaction of oceanic and atmospheric processes at an intraseasonal time-scale. It is therefore of first importance to describe the SST intraseasonal variability (ISV) in this part of the basin and understand the mechanisms at stake, in particular whether ocean and atmosphere are coupled.

Along the Equator, Athié and Marin (2008) show that the strongest SST ISV is dominated by 20–40 and 10–20-day time-scales, respectively west and east of 10°W in boreal spring and summer. Many studies of the equatorial Tropical Instability Waves (TIW) signal have defined them as the main driver of SST ISV in the central tropical Atlantic region (e.g. Seo *et al.*, 2007; Giordani *et al.*, 2013; Jouanno *et al.*, 2013). They demonstrate the major role of TIW-induced horizontal advection and vertical mixing in the generation of intraseasonal SST anomalies (thereafter SSTAs). The near-surface atmosphere has also been shown to be forced by the TIW-induced SSTAs according to Caltabiano *et al.* (2005). The latter show particularly that local intraseasonal surface wind anomalies appear to be explained by the SW mechanism. However, the LN mechanism is also at stake, as shown in the present article. East of 10°W, de Coëtlogon *et al.* (2010) suggest that the ISV exhibits the signature of a negative SST–surface wind feedback, which increases a quasi-biweekly variability in both parameters. Using forced oceanic simulations, they show that the main drivers of equatorial SSTAs are horizontal advection, and vertical entrainment and diffusion. They also show evidence that both SW and LN mechanisms influence the surface wind.

Along southern African coasts, Hermes and Reason (2009) reveal that the SST ISV is maximized at the Angola-Benguela front (hereafter ABF). They also show that ISV over this region is dominated by 20–30 and 30–64-day regimes for the wind and SST respectively, with some overlap. Although, authors provide elements suggesting that the fluctuations of the 'Angola low' generate the wind anomalies and SST ISV is driven by Ekman dynamics, they however do not analyse the physics of the interaction mechanisms.

Further south (off Namibia near 26°S) a secondary SST ISV maximum of smaller extension is studied by Goubanova *et al.* (2013). They detect two dominant regimes: a 2–30-day regime, and a 30–90-day regime. Also without exploring the SST–wind interaction mechanisms, they suggest that SSTAs remain controlled by Ekman dynamics. Furthermore, they reveal that the large-scale atmospheric forcing comes from the intraseasonal component of the Antarctic Oscillation (AAO), which may be influenced by the passing of the Madden–Julian Oscillation (MJO: Madden and Julian, 1971) according to Foltz and McPhaden (2004). The latter hypothesize that the MJO may propagate from the Indo-Pacific Ocean into the Atlantic and affect the AAO and the North Atlantic Oscillation (NAO) in the Southern and Northern Hemispheres respectively. Cassou (2008) argues that the MJO penetration along the mean storm track in the North Atlantic (40–60°N) is associated with dominant anticyclonic synoptic-scale wave breaking (AWB) known as a precursor of the NAO+ regime (from a lag of 10–15 days onwards). Pohl and Fauchereau (2012) suggest that the preferred range of variability of the AAO is intraseasonal, with 34% (62%) of the total AAO variability confined in the 35–63 (18–117) day frequency band, and can have a strong impact on the regional climate variability of

the Southern Hemisphere. The possible influence of the MJO on tropical Atlantic SST ISV is thus briefly investigated in this article.

Moreover, as discussed in Yamagata and Iizuka (1995) and in Doi *et al.* (2007) respectively from climatology and interannual perspectives, planetary coastal trapped waves (hereafter CTWs) form another important potential forcing mechanism along the African coasts. They exhibit intense ISV at least between about 15° North and South (Polo *et al.*, 2008). However, statistically significant evidence of their expected impact on SST ISV is still sparse. Goubanova *et al.* (2013) show that near 26°S at the coast the energy of the second baroclinic mode peaks at intraseasonal periods very close to those of SST. (Wade *et al.*, 2015) find maximum correlation between SSH and SST ISV near the location of African coastal upwelling fronts. He provides evidence that a CTW of standard amplitude can cause an SSTA of about 0.5 °C in this frequency band, depending on the season.

The main goal of the present study is to provide a synthesis and statistically robust view of the largest SST fluctuations at intraseasonal time-scales (i.e. in the 10–90 day range) in the tropical Atlantic, and investigate their nature and main causes. We are particularly interested to know whether signals of an active air–sea coupling, as the one found in the equatorial upwelling east of 10°W (de Coëtlogon *et al.*, 2010), can be detected in the other upwelling systems. Documenting the oceanic ISV is indeed particularly important in view of improving knowledge of the ecosystem affected by coastal upwelling and of the marine resources, especially at a time-scale of a few weeks, since it could offer precious predictability skill.

The article is organized as follows. Datasets and methods are presented in section 2, along with the identification of maximum SST ISV locations. Characteristics of the latter and their possible origins and/or coupling with the atmosphere are described in the fronts of eastern equatorial, Angola-Namibia and Senegal-Mauritania upwellings respectively in sections 3, 4 and 5. A summary and short discussion is presented in the last section.

2. Data and methods

2.1. Data

Surface wind vectors are provided by the QuikSCAT (Quick Scatterometer) satellite (Liu *et al.*, 2000) available from the Remote Sensing Systems website (http://www.remss.com) as 3-day running means on a 0.25° × 0.25° grid between 2000 and 2009. A two-dimensional cubic-spline interpolation first fills the gaps due to clouds for each available day, and then a linear temporal interpolation at each grid point completes the 15 missing days over the decade.

The high-resolution SST product developed using optimum interpolation, the Advanced Very High Resolution Radiometer (AVHRR) infrared satellite SST data, and *in situ* data from ships and buoys (Reynolds *et al.*, 2007) have been retrieved thanks to the US National Oceanic and Atmospheric Administration - National Climatic Data Center (NOAA-NCDC) ftp site (http://www.ncdc.noaa.gov) with 0.25° spatial grid and daily resolution.

In addition, SSH from Topography EXperiment (TOPEX/Poseidon) altimetry measurements with 0.5° horizontal resolution and 7-day time resolution produced and distributed by Archiving, Validation and Interpretation of Satellite Oceanographic data (AVISO) is also used, as well as NOAA daily outgoing long-wave radiation (OLR) data (ftp://ftp.cpc.ncep.noaa.gov), and KNMI daily climate indices (NAO, AAO; http://climexp.knmi.nl/selectdailyindex.cgi?id=someone@somewhere).

Reanalysis from the Climate Forecast System Reanalysis (CFSR: Saha *et al.*, 2010) are retrieved from the National Centers for Environmental Prediction (NCEP) site (www.ncep.noaa.gov). A distinctive characteristic of CFSR is that it is performed with a coupled ocean–atmosphere model, which is shown to better describe the air–sea interaction in the eastern tropical Atlantic than the ERA-Interim (European Centre for Medium-Range Weather Forecasts Re-Analysis: de Coëtlogon *et al.*, 2014). The data are available on a 0.5° × 0.5° horizontal grid, with vertical atmospheric profiles retrieved on 27 levels from 1000 to 100 hPa. Daily means of the 6-hourly parameters are used over the 2000–2009 decade.

Table 1. Acronyms, definitions and longitude–latitude boundaries of SST indices used in this study.

Indices acronyms	Full names	Areas
NWCTI	North-Western Cold Tongue Index	11–15°W/0.5–2.5°N
NECTI	North-Eastern Cold Tongue Index	3–7°W/0.5°S–1°N
ABFI	Angola-Benguela Front Index	225 km offshore/15–18°S
SMFSI	Senegal-Mauritania Front Southern Index	17.5–19°W to 11–14°N
SMFNI	Senegal-Mauritania Front Northern Index	225 km offshore/19.5–22°N

2.2. Methods

2.2.1. Building indices of regional ISV

In order to identify the location and season of maximum SST ISV, SST is first high-pass filtered using a Lanczos filter with a 90-day cut-off, thereby removing seasonal and interannual time-scales. The root mean square (r.m.s.) of the remaining SST anomaly (SSTA) is then performed to evaluate the SST ISV evaluation. Monthly climatological values of the SST ISV are computed, and their maximum selected (Figure 1(a)).

Not surprisingly, the anomalies of largest variance within tropical areas are found in the frontal regions of main upwelling, where the mean SST gradients are relatively strong: the equatorial upwelling fronts (0–15°W), the front of the Canary upwelling (around 18°W and 10–23°N), and the Angola-Benguela front (ABF) (near 12°E and 20 to 10°S). Maximum SST ISV generally occurs in late spring and summer in each hemisphere (i.e. in May–September north of the Equator, and in November–March south of the Equator, Figure 1(b)), when the wind is generally weaker and the ocean mixed layer shallower. Because of a decreased oceanic thermal inertia of the latter, heat fluxes (horizontal and vertical) effects on SST are increased, leading to large anomalies, especially in regions with large SST gradients. For each upwelling region, detailed scans of time–latitude or time–longitude variability of SSTAs are used to determine precisely, areas and times of the year that correspond to maximum ISV. SST and wind averaged in these boxes are thereafter used as indices (see Table 1 for more details).

2.2.2. Surface wind–SST covariance

For the three emphasized regions, two sub-areas of special interest are selected over the Equator, one along the Angolan-Namibian coast, and two off Senegal-Mauritania, leading to a total of five SST indices. Five corresponding surface wind speed indices are also computed, by averaging the surface wind speed in the same boxes (Figure 1). The r.m.s. of each index is normalized to 1. In order to detect time-frequency variations within these indices, wavelet analysis (see details in Torrence and Compo, 1998) with a continuous wavelet transform based on the Morlet function ($w_o = 6$) is used following Goubanova *et al.* (2013). After computing the wavelet transform using daily and full (2000–2009) normalized indices, we average the global power spectrum for each calendar month, thereby documenting the seasonal cycle of variance maximum and frequency ranges. Significance levels are determined from a χ^2 distribution, using a background spectrum defined as a first-order autoregressive

process having the same autocorrelation at lag −1 as our data (Torrence and Compo, 1998).

2.2.3. *Lagged linear regression*

Once a frequency range is identified in one of the SST indices, lagged linear regressions of atmospheric and oceanic fields are performed onto this index. In order to map associated spatial and temporal patterns for the given frequency range, the index and all parameters (atmospheric and oceanic) are band-passed in this specific frequency range (still with a Lanczos filter) before performing the regression. The lagged regression provides useful insight on the linear relationship between SST and the atmospheric circulation, the latter being potentially recognized as a cause (at negative lags) or consequence (at positive lags) of the SSTAs. It consists of computing a simple correlation at each grid point between the lagged anomalous field and the index, weighted by the r.m.s. of the field. We choose to present the anomalous patterns that are linearly correlated with a negative one standard deviation of the index (which amounts to about 1 °C for the five indices, see Figure 1(a)), but as this analysis is linear, opposite patterns are of course just as significant. Only correlations above the 90% significance threshold (meaning that the null hypothesis is rejected with a risk of 10% of being wrong) are shown.

Linear regression maps are shown at different carefully chosen lags, in order to present the most extensive view of the regression patterns for each SST index (Figures 3, 5, 8, 12 and 15). The temporal evolution of the wind–SST interaction is also examined locally, through the lagged regression of the surface wind speed and SST averaged over the same index boxes (Figures 4, 6, 9, 13 and 16). This timing diagnostic is also extended to the three main terms of the oceanic mixed-layer heat budget (see next paragraph for details on how these are estimated).

2.2.4. *Heat budget for the oceanic mixed layer*

The heat budget of the surface mixed layer is computed using ocean and atmosphere parameters from the CFSR (available every 6 h on a 0.75° × 0.75° grid). SST and surface currents are computed by averaging temperature and velocities in the oceanic mixed layer, whose depth h is an output of the reanalysis. As it is computed off-line, this budget must be considered as a first-order estimate. Therefore, we only compute the terms associated with surface heat fluxes and horizontal advection. The rest is considered as the residual, and it is assumed to include all heat fluxes through the base of the mixed layer (vertical entrainment and diffusion) as well as subgrid-scale processes. Intraseasonal anomalies are performed as defined previously (i.e. high-pass filtered under 90-day periods). The tendency equation for SSTA (denoted as T') is (see for example Peter *et al.*, 2006; de Coëtlogon *et al.*, 2010):

$$\frac{\partial T'}{\partial t} = \frac{Q'_{\mathrm{h}} - Q'_{\mathrm{a}} - Q'_{\mathrm{r}}}{\rho_{\mathrm{o}} C_p h},$$

where $\rho = 1023$ kg m^{-3}; $C_p = 3985$ J kg^{-1} K^{-1}; h, the mixed-layer depth; Q'_{h}, the anomaly of net surface heat flux; Q'_{a}, the anomalous horizontal advection (i.e. the advection of SSTA by the mean current, plus advection of the mean SST by anomalous currents); and Q'_{r}, the anomalous residual. Q'_{h} and Q'_{a} are formulated as follows:

$$Q'_{\mathrm{h}} = LHFL' + SHFL' + LWR' + NPSWR',$$
$$Q'_{\mathrm{a}} = u'\frac{\Delta \bar{T}}{\Delta x} + v'\frac{\Delta \bar{T}}{\Delta y} + \bar{u}\frac{\Delta T'}{\Delta x} + \bar{v}\frac{\Delta T'}{\Delta y},$$

with $LHFL'$, $SHFL'$, LWR' and $NPSWR'$ representing respectively the latent, sensible, long-wave, and non-penetrative short-wave radiative heat fluxes. $\bar{u}$ and $\bar{v}$ are the mean zonal and meridional surface current in the corresponding period, u' and v' their anomalies. $\bar{T}$ is the mean SST in the corresponding period and T' its anomaly. Flux values are taken positive downward, i.e. a positive surface heat flux anomaly warms up the ocean and damps a cold SST anomaly. Finally, as in de Coëtlogon *et al.* (2010), $NPSWR'$ is computed as follow:

$$NPSWR' = SWR'(1 - 0.58 * \exp(-h/0.35) + 0.42 * \exp(-h/23))$$

where SWR' is the short-wave radiative flux.

2.2.5. *Wave-tracking method description*

Wave tracks are defined along the Equator, as well as northward or southward along the African coast in order to document potential oceanic equatorial Kelvin waves (EKWs) and CTW propagation. The distance between two grid points is 0.25° (∼25 km) following the resolution of Reynolds SST. In the north, the track moves westward along the Guinean coast and continues northward up to 30°N, having twice as many track points than the south, where the track runs down to 25°S along the southern African coast. Note that both north and south wave tracks share the first 270 points corresponding to the equatorial Atlantic. As in Polo *et al.* (2008), following the coastline along different isobaths (0, 200, 400, 1000 m) does not make substantial differences, and no remarkable property changes are found (not shown). Here, the term 'Kelvin wave' refers to equatorial and coastally trapped propagation, even though the coastal wave may be a mix of Kelvin and topographic waves. SSH, SST and surface wind signals are built along these tracks, and their linear lagged regression performed onto the coastal SST indices.

3. The equatorial zone

Figure 2(a) shows the seasonal r.m.s. of intraseasonal anomalies of SST and surface wind, as well as the monthly SST climatology along the Equator (2°S–2°N). Maximum SST variance is observed from May to August. During this period, as documented in previous studies (e.g. Gu and Adler, 2004; Okumura *et al.*, 2006; Caniaux *et al.*, 2011; Giordani *et al.*, 2013), SST fluctuations are dominated by the development of a seasonal cold tongue resulting from a shallower thermocline and thinner mixed layer induced by stronger southeasterly trade winds. As a consequence, two maxima of SST intraseasonal variance frame the Equator in the central and eastern basin in May–August: one between 11 and 15°W, and another one between 3 and 7°W (Figure 2(a)). Time–latitude plots show that their positions coincide with the northern front of the cold tongue, with quite a large meridional extent between 0.5 and 2.5°N for the western index (Figure 2(b)), and between 0.5°S and 1°N for the eastern one (Figure 2(c)). Two areas for the equatorial indices are therefore selected: 11–15°W/0.5–2.5°N (thereafter named '*North-Western Cold Tongue Index*' or NWCTI), and 3–7°W/0.5°S–1°N (as '*North-Eastern Cold Tongue Index*' or NECTI). Note that these two locations correspond respectively to the poles of the first and second modes found when performing empirical orthogonal function (EOF) decomposition with intraseasonal SSTAs over the eastern tropical Atlantic (not shown). An interesting feature is that the maximum intraseasonal variance of the wind velocity is also found roughly over these two areas (around 1 m s^{-1}, Figure 2(b,c)), suggesting three possibilities: SST passively responds to wind fluctuations, wind passively responds to SST, or SST and wind are coupled.

Wavelet analysis of SST indices shows that they both exhibit maximum variance in June–July. The meridional SST gradient is largest in boreal summer, and SSTAs induced by the displacements of the front are most variable also during this period. The NWCTI SST power spectrum is significant between 20- and 70-day periods (Figure 2(d)), whereas for the NECTI this range extends down to 10-day. In the NCWTI, the variance peaks

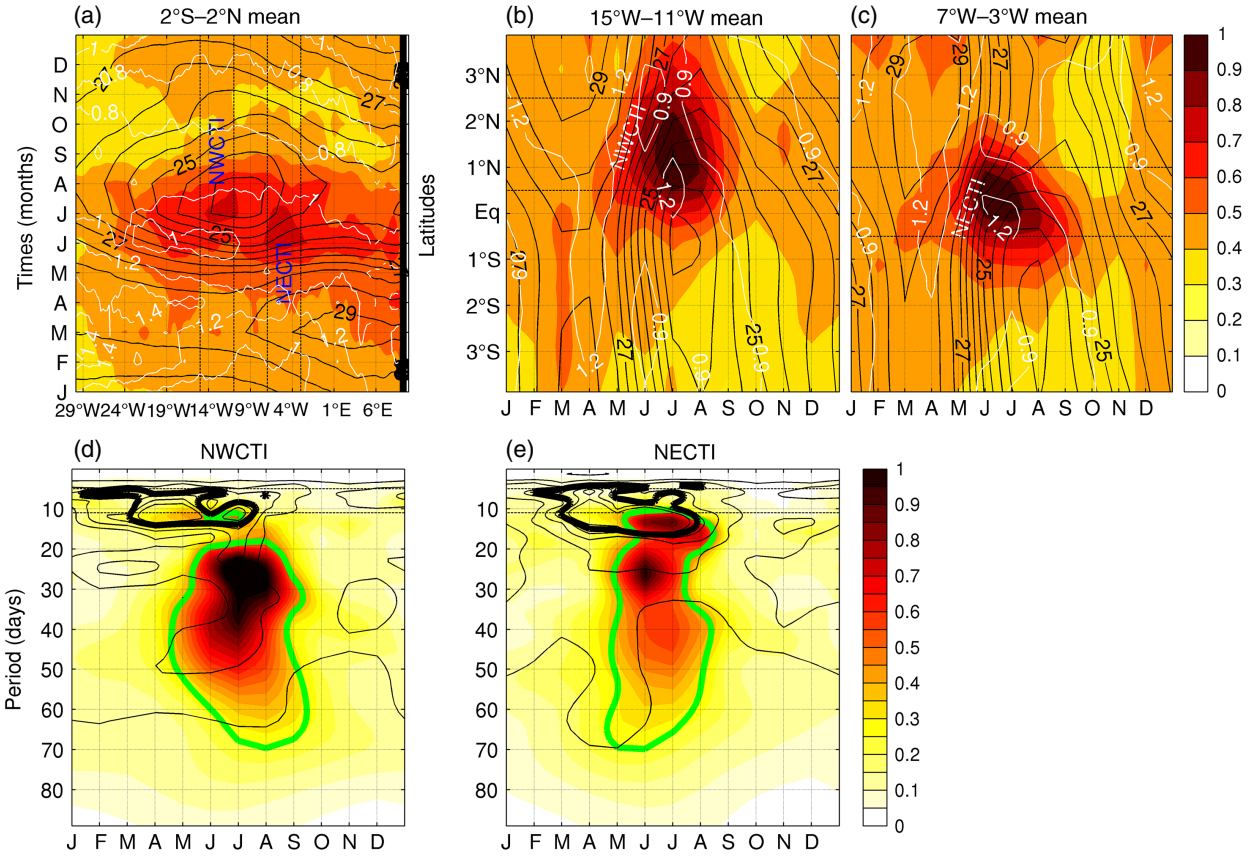

Figure 2. Monthly climatology (2000–2009), averaged between (a) 2°S and 2°N, (b) 15°W and 11°W and (c) 7°W and 3°W, of SST anomaly r.m.s. (shading, intervals of 0.1 °C), SST (black contours, intervals of 0.5 °C), and surface wind anomaly r.m.s. (white contours, intervals of 0.2 m s^{-1}). (d,e) Normalized wavelet power spectrum of NWCTI and NECTI SST (shading) and wind (black contours, intervals of 1 unit) indices. Heavy green (resp. black) contours show the 90% confidence level for the SST (resp. wind).

around 25-day in June–July. A peak around 25-day is also found in the NECTI, but weaker and only in July, together with another peak centred around 15-day in June–July (Figure 2(e)). Both wind indices (NECTI and NWCTI) present significant peaks from 8- to 18-day between March and July (Figure 2(d,e), black contours), with maximum values around 10-day in April for the NWCTI, and 15-day in May–July for the NECTI. No significant peaks are found in the wind spectrum between 20 and 70 days (Figure 2(d,e)). SST low frequencies (20–70 days) in these two regions must then originate from ocean dynamics alone. In April–May, the 10-day peak found in the two wind indices does not match any significant peak in the oceanic spectrum. In June–July two SST–wind covariabilities are observed around 10-day (NWCTI) and 15-day (NECTI) periods. They support the possibility that they derive from active air–sea interaction. This hypothesis is explored through lagged linear regression of 10–20-day band-passed parameters. In addition, lagged regressions are also performed on the 20–60-day band-passed parameters, in order to investigate the potential influence of SST on surface wind at this frequency range. Regressions in the two frequency ranges exhibit very similar patterns for both indices. Although no corresponding significance is found in the local spectrum, the wind response to SSTAs could indeed be spatially shifted. We thereafter focus only on the most variant ranges in the SST spectrum for each index: 20–60-day in June–July for the NWCTI (preferred over 20–70-day, because slightly more significant) and 10–20-day in May–June–July for the NECTI.

3.1. *Lagged linear regressions on the NWCTI*

Figure 3 shows the regression on the NWCTI. SSTAs present a very clear westward propagation feature, with a period of about 35 days and speed of 30–60 cm s^{-1}. These properties are very close to the characteristics of TIW (e.g. Düing *et al.*, 1975; Qiao and Weisberg, 1995; Wainer *et al.*, 2003; Caltabiano *et al.*, 2005; Jochum *et al.*, 2005; Bunge *et al.*, 2006, 2007; Athié *et al.*, 2009). As discussed by Athié *et al.* (2009), and further confirmed by Jouanno *et al.* (2013), the oceanic TIW signature appears as mixed Rossby–Yanai waves and controls the equatorial SST fluctuations west of 10°W in boreal spring and summer.

Note that in addition to the temporal high-pass filtering, sea-level pressure (SLP) is also spatially filtered before computing the linear regression following Chelton *et al.* (2001, 2005). This allows us to remove all large-scale features having longitudinal wavelengths larger than 10°. Positive (negative) SLP anomalies clearly coincide with negative (positive) SSTAs, suggesting that small-scale SLP perturbations are controlled by local SSTAs (Figure 3). Wind anomalies appear sometimes clearly directed from high to low pressure centres, which corresponds to the signature of the LN mechanism (O'Neill *et al.*, 2010b). However, in agreement with Caltabiano *et al.* (2005), the SW mechanism appears here as the dominant one. Indeed, as the meridional component dominates the mean wind field in this region, its response to SSTAs follows a southward (northward) acceleration over colder (warmer) water, causing divergence (convergence) over the negative (positive) equatorial SSTAs. Also, locally averaged observed SST and surface wind projection on the NWCTI (Figure 4(a)) clearly shows that wind anomalies vary in phase with SSTAs, meaning that the delay of wind response to SSTAs is very short (less than 1 day), which is coherent with the SW mechanism (de Coëtlogon *et al.*, 2014).

Oceanic heat budget analysis suggests that the main term controlling the growth and decay of the SSTAs is the horizontal oceanic advection, followed by the residual (assumed to correspond mostly to vertical entrainment and diffusion, Figure 4(b)). Surface heat fluxes are totally negligible here. These results (from off-line heat budget with CFSR oceanic parameters) confirm previous studies (Seo *et al.*, 2007; Giordani *et al.*, 2013; Jouanno *et al.*, 2013), with on-line heat budget. Although significantly impacted, the TIW-induced wind perturbation

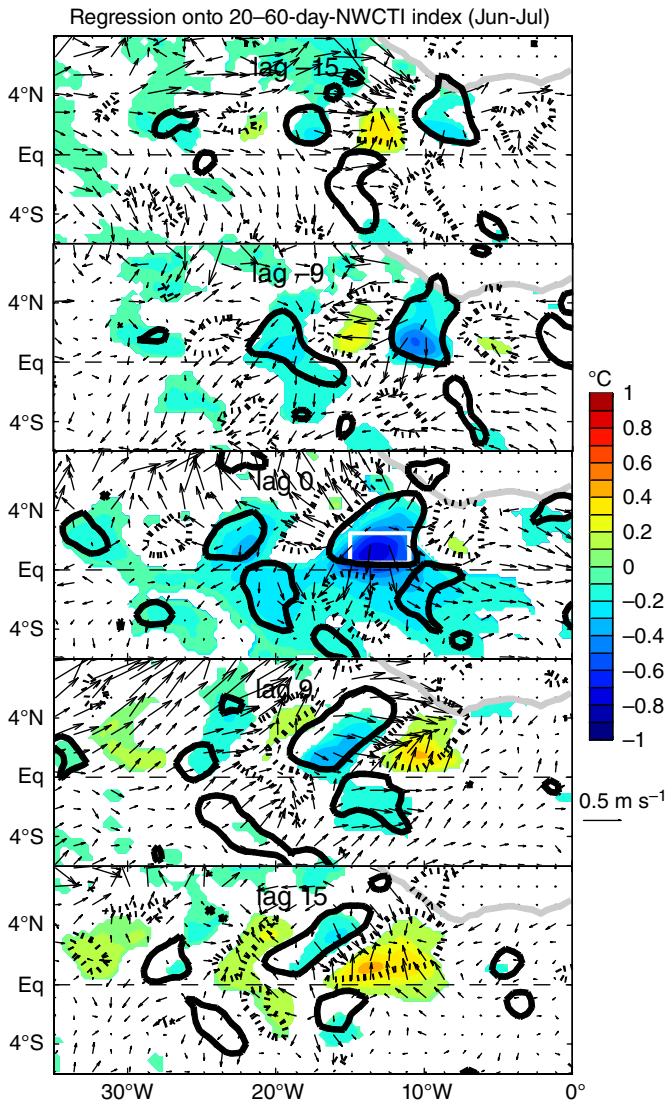

Figure 3. Lagged regressions of Reynolds SST anomaly (shading, °C, intervals of 0.1 °C), QuikSCAT surface wind anomaly (arrows) and CFSR SLP anomaly (contours, intervals of 1 Pa) onto NWCTI. All time series have been band-pass filtered between 20 and 60 days before the regression, and only months from June to July are selected. Only 10% significant SST and wind anomalies are plotted. The heavy black contour represents the 10% significant SLP anomaly, plain for positive, dashed for negative. The NWCTI leads at negative lags. Lags are in days, from top to bottom. The white box at lag 0 indicates the index box.

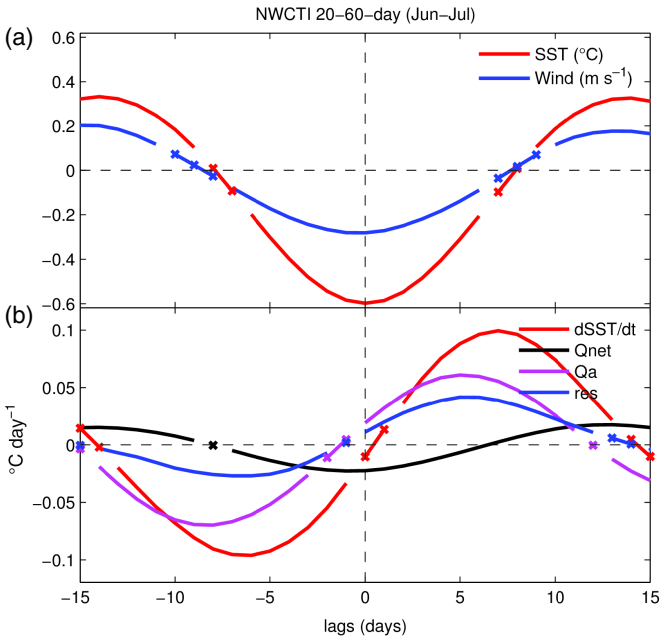

Figure 4. Lagged regressions on the NWCTI of: (a) Reynolds SST (red, °C) and QuikSCAT surface wind (blue, m s^{-1}), (b) CFSR heat-budget terms (°C day^{-1}): tendency (red), net heat flux (black), total horizontal advection (magenta), and residual (blue), averaged in the NWCTI area. Crossed parts of curves represent non-significant values (using the same test as in Figure 3). All time series have been band-pass filtered between 20 and 60 days, and only months from June to July are selected.

appears therefore not favourable to wave-train propagation through air–sea coupling. The wind anomalies created by SSTAs tend to damp the latter through horizontal advection. For example, the cold SSTA around 13°W–1°N at lag 0 decreases the overlying wind (Figure 3) and then the northward advection of surface water around the front, leading to damping in turn the cold SSTA (from −1 °C at lag 0 to 0 °C at lag 8).

3.2. *Lagged linear regressions on the NECTI*

Figure 5 shows the regression of SST, SLP and surface wind anomalies on the 10–20-day band-passed NECTI in May–June–July. At lag −6 (i.e. 6 days before the coldest SSTAs), significant surface wind anomalies are found in the eastern equatorial Atlantic, together with a characteristic pattern in the SLP (Figure 5). This means that the equatorial SSTAs (which by definition reaches about −1 °C at lag 0) are mainly cooled by wind acceleration, driven 6 days earlier by an anticyclonic pressure pattern in the southern Subtropics. The most important processes in this cooling are the residual (supposed to mainly represent the vertical mixing and diffusion in the heat budget equation), and the horizontal advection (Figure 6). Between lags −10 and −3, the wind is stronger than normal, which increases the vertical oceanic mixing and drags colder waters northwestward from the cold tongue. This is in agreement with previous studies, which show that in this region the wind creates SSTAs mostly through enhanced vertical diffusion and horizontal advection (de Coëtlogon *et al.*, 2010; Jouanno *et al.*, 2011, 2013; Giordani *et al.*, 2013).

After lag −3, the wind anomaly weakens because the SST cools down, probably through both LN and SW mechanisms (de Coëtlogon *et al.*, 2014). This reduces the horizontal advection and the residual after a few days. The cold SSTA reaches a minimum at lag 0, before damping within a few days (Figure 6). The wind is the weakest at lags 1 or 2 (i.e. in 1 or 2 days after the minimum of SSTA), with southward anomalies (Figure 5). The surface wind therefore responds to the SST in 1 or 2 days, while the SST responds in 5–6 days. This SST–wind negative feedback leads to an oscillation with a half period of about a week.

The strong quasi-biweekly variability of both SST and surface wind observed in the equatorial front region east of 10°W would then largely come from an air–sea coupling around the Equator, as discussed in de Coëtlogon *et al.* (2010, 2014), rather than from TIW-like wave dynamics which raise the variance of the 20–60-day periodicities further west (Figure 2(e)). The NWCTI and NECTI therefore involve both LN and SW mechanisms for the wind response to SST fluctuations, and both horizontal advection and vertical mixing for the SST response to wind. However, east of 10°W (NECTI), the air–sea coupling is very strong, which explains a dominant 15-day variability peak in May–July for both SST and wind (Figure 2(e)), while this peak is more modest west of 10°W (NWCTI), where the wind responds rather passively to the TIW-like SSTAs in the 20–60-day periodicity range (Figure 2(d)).

4. The Angola-Benguela front

In this section, we focus on the offshore Angola-Namibia region, especially the ABF. The maximum of SST ISV extends as far as 200–300 km offshore (Figure 1). The intraseasonal r.m.s. of SST is therefore averaged in the 225 km zone off the coast before performing its time–latitude seasonal cycle (Figure 7(a)). Seasonal cycles of SST mean and wind r.m.s. are also plotted,

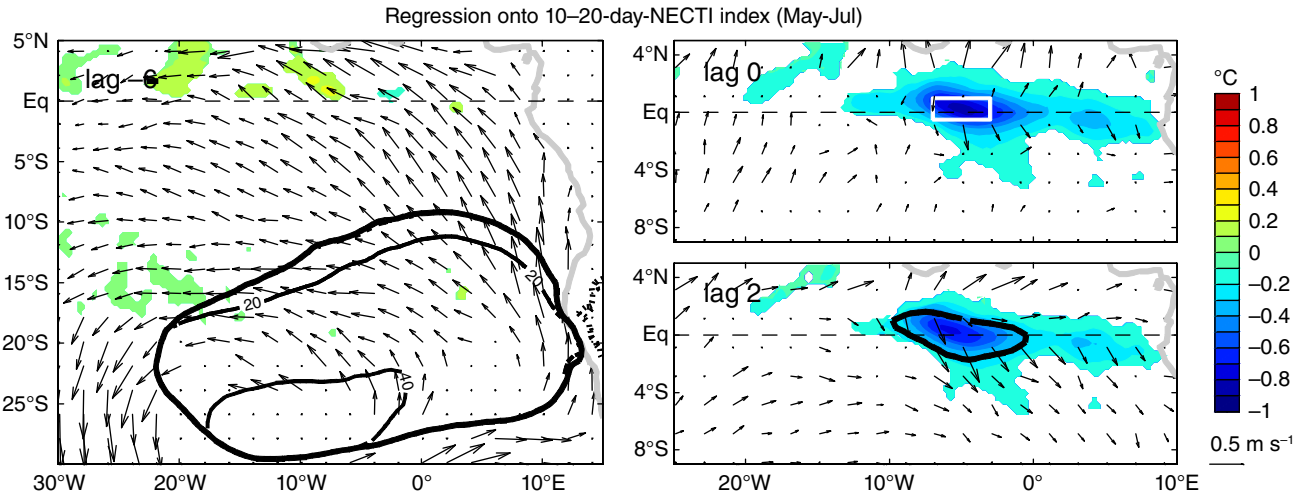

Figure 5. Same as Figure 3, but for the NECTI: all time series have been band-pass filtered between 10 and 20 days, and only months from May to July are selected.

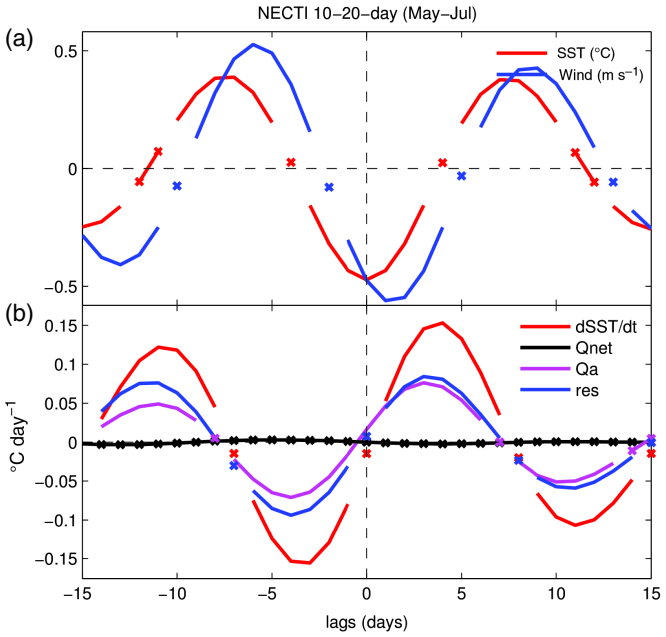

Figure 6. Same as Figure 4, but for the NECTI: all time series have been band-pass filtered between 10 and 20 days, and only months from May to July are selected.

allowing for comparison of the SST ISV with the climatological position of the SST front and local wind ISV.

At the ABF, an SST r.m.s. of up to 1.1 °C is found from December to June around 17°S, but the maximum wind ISV occurs between June and September. This seasonal shift between SST and wind peak variance appears more clearly in the wavelet analysis of the SST and wind indices averaged between 15 and 18°S in the 225 km zone off the Angolan-Namibian coast, where the SST ISV is strongest (Figure 7(b)). The SST index (thereafter '*Angola-Benguela Front Index*' or ABFI) exhibits significant variance between 30 and 80 days from December to June, with apparently distinct signals around 40- and 55-day periods, while no clear significant peak is found in the wind spectrum during this period at these time-scales.

The seasonal shift found in maximum variances (in June–September for the wind, in December–July for the SST) suggests that the wind does not significantly force SST. However, SSTAs variance results from the intensity of the background low-frequency SST gradients and mixed-layer depth. The horizontal gradient is indeed maximum in November–June (4 °C over the ABFI latitudinal extension, instead of 3 °C from July to October, Figure 7(a)), as is the vertical gradient, since it is a frontal region of outcropping isotherms. Therefore wind anomalies, even weak, could produce strong SSTAs in this period (see Goubanova *et al.* (2013) for more details). On the other hand, Polo *et al.* (2008) and Goubanova *et al.* (2013) find that the climatological amplitude of EKWs and CTWs is also larger during this period. SST fluctuations could then also be remotely forced through EKWs and CTWs. These two scenarios are explored here below.

Atmospheric and oceanic patterns associated with the 30–80-day regime during ISV maximum (from December to June) are investigated with lagged linear regressions (Figure 8). The cold SSTAs develop within about 2 weeks, together with strong south-easterly along-shore wind anomalies driven by large-scale anticyclonic SLP anomalies, with one centre near 5°E/22°S and a second one at midlatitudes (see lag −9). These SLP anomalies (thereafter called 'SLP ABFI') remain stationary for about 8 days (only lags −9 and −4 are shown here) and increase until their two significant centres connect with each other. The lead and lag correlation between the AAO and ABF indices presents a significant (negative) correlation around lag 0, suggesting that the AAO could partly control the SST ISV off Angola-Namibia (see Figure 17(a) later). The large positive correlation around lag 15–20 days may then translate into a link between ABF and AAO indices, with an overall periodicity of 30–40 days. Although even the ABFI used here differs from the index studied in Goubanova *et al.* (2013), this result confirms their hypotheses affirming that the ISV of the anticyclone signal corresponds to the intraseasonal component of the AAO.

In addition, Figure 17(b) (see later) shows evidence of interaction between the MJO and the SST ISV off Angola-Namibia, through a lead/lag correlation between the ABFI and the MJO index from Slingo *et al.* (1999) (i.e. the first principal component time series of the 30–70-day OLR in the eastern tropical Indian and western tropical Pacific (60°E–90°W, 30°S–30°N) in December–June). A large correlation is found when the MJO index leads the ABFI by about 10 days (positive value), and when the MJO index lags by 6–7 days (negative value), translating into a periodicity of 30–40 days known to characterize MJO variability. Also, the AAO is probably influenced by the MJO, as can be seen in Figure 17(b) (see later). The MJO index is significantly correlated with the AAO index when the latter lags by about 10 days. Moreover, the SLP ABFI is close to the anticyclonic pattern that forces the eastern equatorial SST index (or NECTI, Figure 5, lag −6), supposed to correspond to fluctuations of the St Helena anticyclone. Both patterns are indeed centred on the same latitude (20°S), but the SLP ABFI extends much less westward (5°E instead of 20°W). The ABFI would therefore be influenced by the three patterns (AAO, MJO and St Helena anticyclone fluctuations) possibly interacting in a way leading to the SLP ABFI pattern strangely persisting for more than 1 week.

The lagged linear regression of local indices of SST and wind speed on the ABFI shows that the wind acceleration starts about 24 days before the minimum of the SSTAs (Figure 9(a)). Maximum correlation between the SST and wind speed anomalies

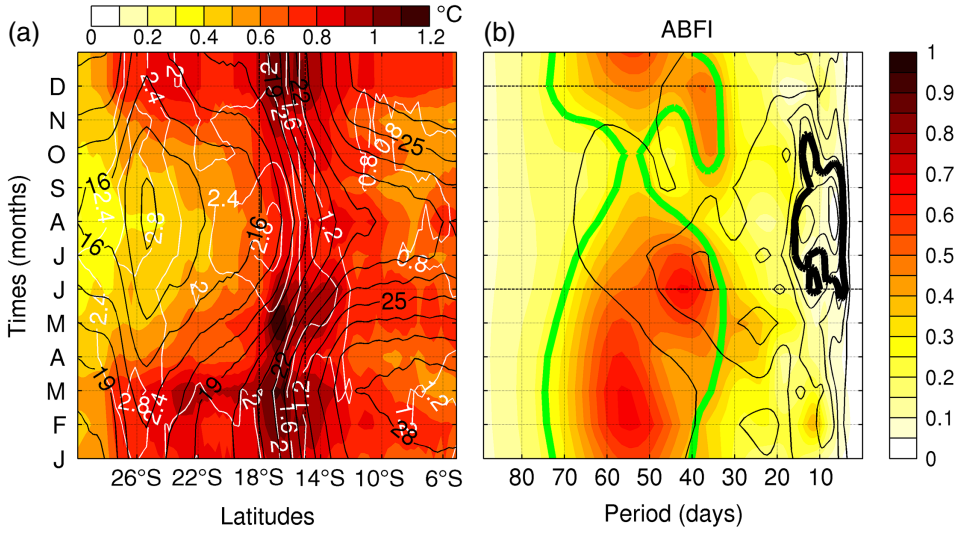

Figure 7. (a) Seasonal cycle of the r.m.s. of equatorial SST (shading, °C) and wind (white contours, intervals of 0.2 m s^{-1}) intraseasonal anomalies, averaged in the 225 km band along the African coast. (b) Normalized wavelet power spectrum of ABFI SST (colours) and wind (black contours) indices. Heavy green (resp. black) contours show the 90% confidence level for the SST (resp. wind).

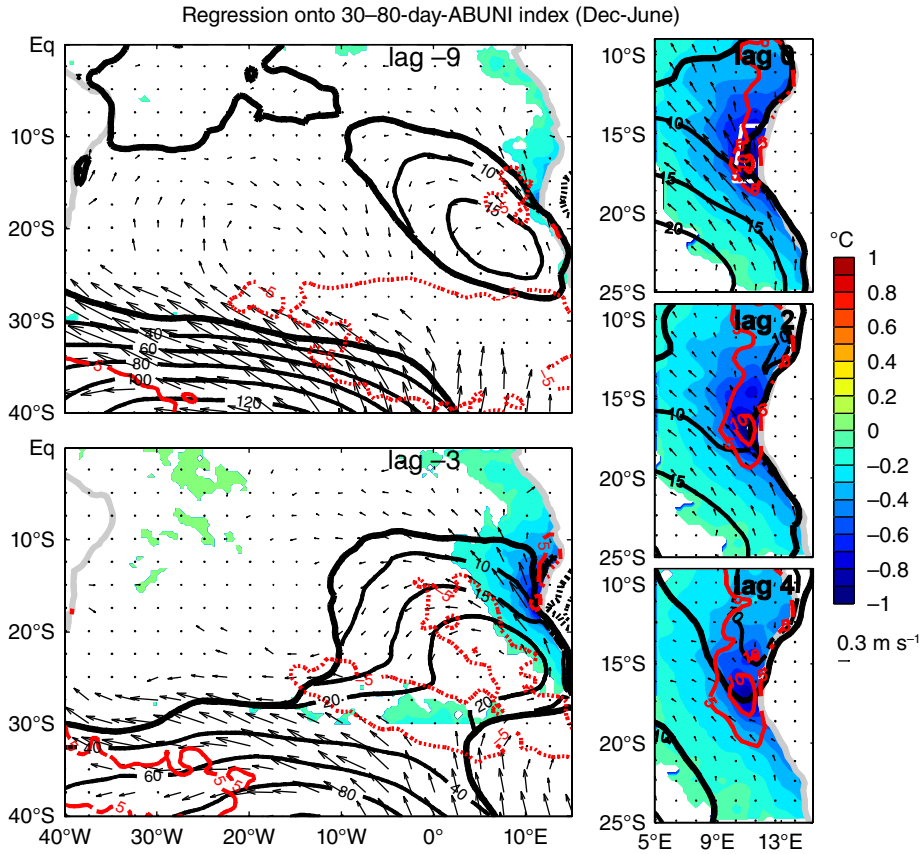

Figure 8. Same as Figure 3, but for the ABFI: with SLP anomalies in black contours (intervals of 5 hPa) and latent surface heat flux anomalies (red contours, intervals of 5 W m^{-2}, plain for positive, dotted for negative). Heat fluxes are positive downward. All time series have been band-pass filtered between 30 and 80 days, and only months from December to June are selected.

is observed when the latter leads by 4 days (with a wind stronger than normal by about 0.4 m s^{-1}), confirming that coastal upwelling is forced by wind within 1–2 weeks. When the SSTA is the coldest (around lag 0), it is clearly damped by the net surface heat flux (a positive heat flux anomaly indicates a reduced ocean-to-atmosphere heat flux, opposing the SST cooling) in a much more significant way than in the equatorial region (Figure 9(b)). Note that the decomposition of the net surface heat flux into its radiative and turbulent contributions shows that this damping is mostly due to the latent heat flux (not shown). A reduced surface latent heat flux can indeed be due to a colder SST, and/or a more humid near-surface atmosphere (not shown), although the wind is stronger. The contribution of the horizontal advection term is here negligible compared to that of vertical fluxes at the mixed-layer base (the residual), in contrast to the equatorial upwelling fronts. The vertical heat flux at the mixed-layer base is by far the leading actor in the SST cooling. However, this term develops (from lag −20) before the wind acceleration starts (from lag −9 onwards), suggesting that another process such as the remote EKW and CTW influences could also drive the vertical mixing.

To investigate EKW and CTW contributions, lagged regression of the SSH field on the ABFI along the southern wave track off the African coast is performed (Figure 10). Parameters have been band-pass filtered between 30- and 80-day before the regression, and only months from December to June are considered (extending the period from November to June does not change the

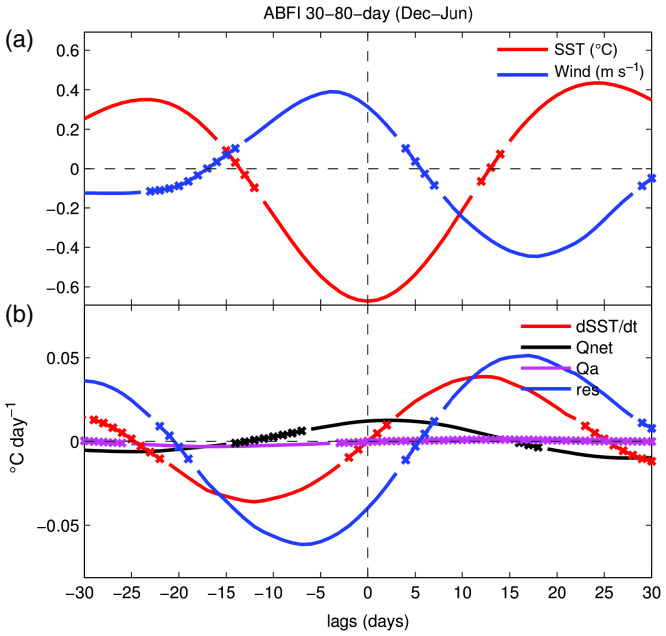

Figure 9. Same as Figure 4, but for the ABFI. All time series have been band-pass filtered between 30 and 80 days, and months from December to June are selected.

results, but lowers their significance). The tracking clearly shows an eastward equatorial and then southward coastal propagation, as far south as 14°S (Figure 10), with a phase speed estimated around 1.6 m s^{-1} and a negative amplitude of almost 1 cm. The signal propagates from near (0°E, 0°N) to the ABFI region in about 5–6 weeks, and displays characteristics very comparable to those of the first baroclinic modes of upwelling EKWs and CTWs described in Polo *et al.* (2008). A significant coastal-wide SSTA of about −0.2°C follows an upwelling wave, from 7 to 26°S (lag 0). SST over SSH ratio is about 0.2 °C cm^{-1}, in agreement with comparable regression coefficients evidenced in observations and wave simulations in the ABF by Wade *et al.* (2015). When the CTW reaches the centre of the ABF, its contribution to the SSTA is thus expected to be around −0.2 °C. This is a consistent part of the total anomaly of −0.7 °C (about 30% of its amplitude, or 10% of its variance).

In return, no clear hint of any wind response to the SSTA is found. At lag 18 (i.e. when wind lags SST by 18 days), the wind has weakened by about 0.5 m s^{-1} (Figure 9(a)), but this takes too long to be attributable to any SST influence through LN or SW mechanisms. On the other hand, as discussed previously, the SSTA seems to feed back onto the atmosphere through damping by surface heat fluxes (mainly the latent heat flux). The latter is indeed widely significant along the coast, around lag 0 (Figure 8, red contours). A very local influence of the SST on the atmosphere could therefore be hypothesized, but this influence is not strong enough to imprint the wind variability significantly in this season (Figure 7(a)).

SST ISV in the southeastern tropical Atlantic basin is then strongest around the ABF (15–18°S) from December to June, with most variant time-scales between 30 and 80 days, following a local coastal wind burst (resp. lull) and the arrival of a CTW, the SSTAs amplitude reaches − (+) 1.1 °C near the coast. Both coastal wind acceleration (deceleration) and upwelling (downwelling) CTW contribute to cool (warm) the local SST, mainly through stronger vertical entrainment and mixing at the upwelling front. The wind burst is associated with a regional-scale anticyclonic SLP anomaly west of 10°W, around the ABF, which results from the interaction of large-scale fluctuations in the St Helena anticyclone, the Antarctic Oscillation, and the Madden–Julian Oscillation. The local wind explains two-thirds of the SSTAs, and the wave the remaining third. Although a feedback of the SST on the surface heat fluxes is detected, no clear influence on the local surface wind is found.

5. The Senegal-Mauritania front

The diagnostic of the SST ISV off West Africa proceeds in the same manner as for that off Angola-Namibia. However, in this region the upwelling core is trapped to the coast only north of 12°N. South of 12°N, it slightly detaches from it, because of the structure of the bathymetry, which is wide and shallow (around 17°W: Roy, 1989; Demarcq and Faure, 2000; Marchesiello and Estrade, 2010). The maximum ISV location is then identified with a time–latitude diagram of SST intraseasonal r.m.s. averaged between 16 and 18°W south of 12°N, and in the 225 km band off the coast north of 12°N (Figure 11). Maximum SST ISV reaches seasonally 0.8 °C and follows the position of the climatological SST front moving in latitude (Figure 11(a)). The front separates the warm water (above 27 °C) of the Atlantic warm pool eastern extension from the cold water (below 20 °C) associated with the southernmost extension of the coastal Canary upwelling system. It is in constant meridional displacement, related to the seasonal migration of the intertropical convergence zone. The SST gradient (roughly 1 °C per degree of latitude or per ∼100 km) is very close to that in the ABF, despite a narrower latitudinal cover. Figure 11(a) also shows that the limits of its migration are northern Mauritania and southern Senegal. Therefore we name it the Senegal-Mauritania Front (SMF hereafter). To better document the air–sea interaction at the front location, which exhibits a large seasonal cycle, two r.m.s. relative maxima are selected in order to build the SST indices: 11–14°N from December to May (thereafter '*SMF Southern Index*', or SMFSI), and 19.5–22°N from June to September ('*SMF Northern Index*', or SMFNI). These maxima also coincide with those in the r.m.s. of the surface wind velocity (larger than 1.6 m s^{-1}), raising then the question of the interaction type (i.e. coupled or not).

The SMFSI SST wavelet spectrum shows a maximum between 30- and 80-day periods (November–May, Figure 11(b)). Significant synchronous peaks for SST and winds are visible around 40-day in DJF, advocating a strong SST–wind interaction. The spectrum maximum for the SMFNI is in the 40–80-day period (June to September, Figure 11(c)). However, no significant wind variability is found at these frequencies, meaning that the SST likely does not influence the wind locally, unless the wind response is shifted by advection.

5.1. *Lagged linear regression on the SMFSI*

Before lag 0, a basin-scale pattern of wind and SLP anomaly dominates the region (Figure 12(a)). It corresponds to a stronger-than-normal Azores anticyclone (centred around 35°W/40°N) with a strong barotropic component. This anticyclone induces anomalously strong trade winds over the West African coast (maximum at lag −9 in the SMFSI box, Figure 13(a)), when the SST starts to cool, off Senegal and Guinea. As shown in Figure 13(b), SSTAs are essentially driven by the residual in the mixed-layer heat budget. This probably corresponds to an increase in the wind-driven vertical mixing and diffusion, as expected of an upwelling regime. Horizontal advection appears to be of small impact on the SMFSI (Figure 13(b)). Regarding SST feedback onto the atmosphere, one can notice a local tilt in the anomalous SLP pattern as early as lag −7 (Figure 12). This suggests that the local positive SLP anomaly in the SMFSI box (maximum at lag 4) could correspond to an adjustment of the pressure to the colder water below, through a local positive net surface heat flux anomaly (seen in Figure 13(b)). However, there is no obvious wind response to the SST anomaly (Figure 12, lags 0 and 4). Local SST and wind speed regression on the SMSFI exhibits 12 days lag between each of their maxima, too long to suggest the SW mechanism (Figure 13(b)). In addition, no significant gradient in SST or SLP anomalies (not shown) are found, meaning that no LN mechanism could be detected. The wind anomalies appear therefore controlled by the large-scale atmospheric circulation in the North Atlantic in agreement with the results found in Dieng *et al.* (2014). Note that this large-scale

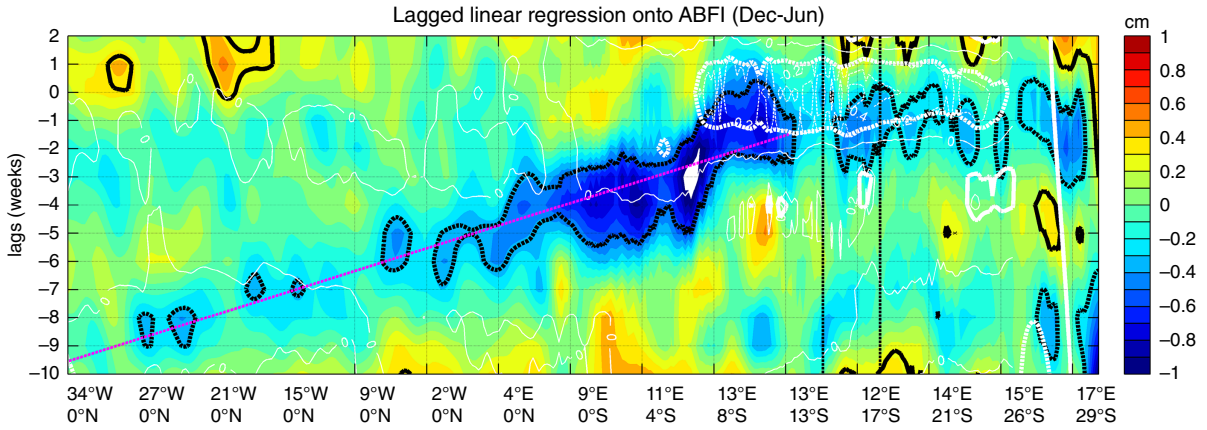

Figure 10. Lagged linear regression onto ABFI of the tracked AVISO SSH (shading, in cm) and Reynolds SST (white contours, intervals of 0.2 °C) anomalies along the Equator (eastward) and the African coast (southward). Heavy black and white contours show the 90% confidence level for SSH and SST anomalies respectively. The black dotted lines indicate latitudinal limits of index area; the magenta one indicates the slope of the EKW. Only months from December to June are selected.

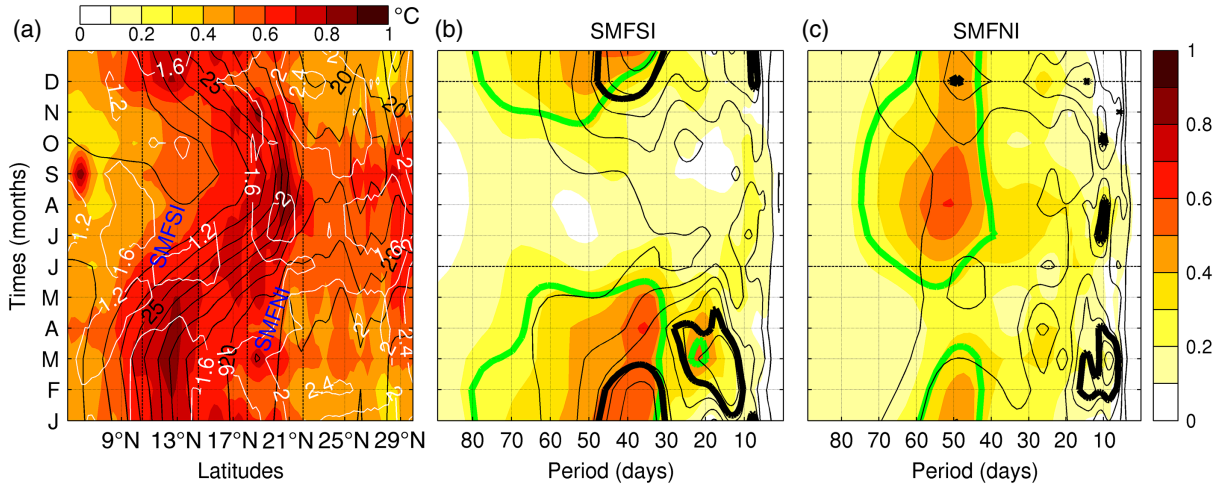

Figure 11. Same as Figures 2 and 7, but (a) for parameters averaged in the 225 km band along the African coast, and the normalized wavelet power spectrum of (b) the SMFSI and (c) the SMFNI.

circulation in the North Atlantic could be connected to the NAO intraseasonal oscillation. Lead/lag correlation between the SMSFI and the NAO shows a large negative and significant correlation around lag −12 (Figure 17(a)). A positive phase of the NAO (with stronger trade winds) would then force an intensification of the southern Senegal-Mauritania upwelling about 12 days later. Figure 17(b) (see later) also shows a significant correlation at lag −20 in the MJO/NAO correlation, meaning that a positive MJO would partly force a positive NAO 20 days later. However, the MJO influence on intraseasonal NAO variations does not appear to have an impact on frontal SST ISV, since no significant correlation is found between MJO and SMSFI.

Regarding a possible oceanic wave forcing along the West African coast, a clear CTW sea-surface height anomaly (SSHA) signal emerges during the November to January period (Figure 14). Its speed and amplitude (about 1 m s^{-1} for 1–2 cm) are in agreement with those evidenced by Polo *et al.* (2008). Since it is negative, this signal could contribute to the upwelling intensification and therefore to the cold SST anomaly. The latter reaches 0.5 °C between November and January (Figure 14), and according to Wade *et al.* (2015), a 2 cm wave is indeed associated with an SSTA of 0.4 °C.

5.2. *Lagged linear regression on the SMFNI*

For the northernmost position of the SMF, cold SSTAs (of nearly 1 °C) are preceded by a strong coastal wind jet, maximum at lag −8 (Figure 15, and see also Figure 13(a), i.e. the regression of the wind speed in the SMFNI box). This jet belongs to a large-scale anticyclonic pattern, slowly moving westward from West Africa along 26°N. Its speed is about 0.6 m s^{-1}, and it is also barotropic. This pattern could be linked with the intraseasonal components of the West African Heat-Low (WAHL) variability described by Chauvin *et al.* (2010).

Figure 16(b) shows that the cooling is started by anomalous advection (dragging southward a colder SST from the north), and followed by a negative (therefore cooling) net surface heat flux. The residual becomes rapidly the dominant cooling term from lag −15 onwards, in agreement with an upwelling regime intensification. At positives lags, the damping is driven by the net air–sea heat flux (up to lag 10, Figure 16(b)) before the residual takes control (from lag 10 onwards). Note that the net air–sea heat flux decomposition shows large domination of the latent heat flux there (not shown). A weaker wind combined with a colder SST and maybe a more humid near-surface atmosphere would all tend to decrease evaporation, explaining the decay of surface heat flux and the SST warming at lag 3 (Figure 16(a)).

In conclusion, off West Africa, two relative maxima of strong SST ISV are found, north and south of 15°N. The southern maximum is most active between November and May in the 30–80-day range of periodicities, and the northern one between June and September in the 40–80-day range (Figure 11). The coastal SSTA in the southern box is induced by an anomalous coastal wind jet that derives from fluctuations of the large-scale circulation in the North Atlantic (Figure 12). Although a significant SST feedback on the SLP anomalies is observed in the SMFSI box (Figure 12, lag 4), no robust signal is found in the local surface wind speed. The SSTA in the northern box also derives from a wind anomaly associated with westward propagation along 26°N of an anticyclonic atmospheric pattern

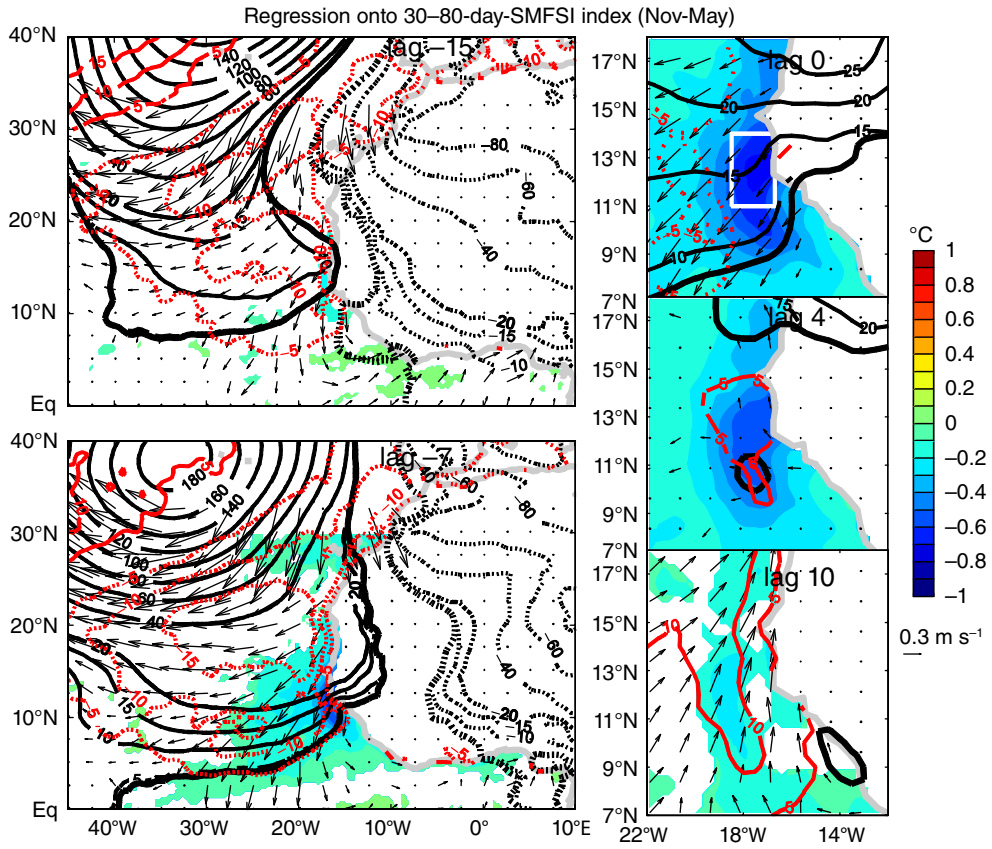

Figure 12. Same as Figure 8, but for the SMFSI: all time series have been band-pass filtered between 30 and 80 days, and only months from November to May are selected.

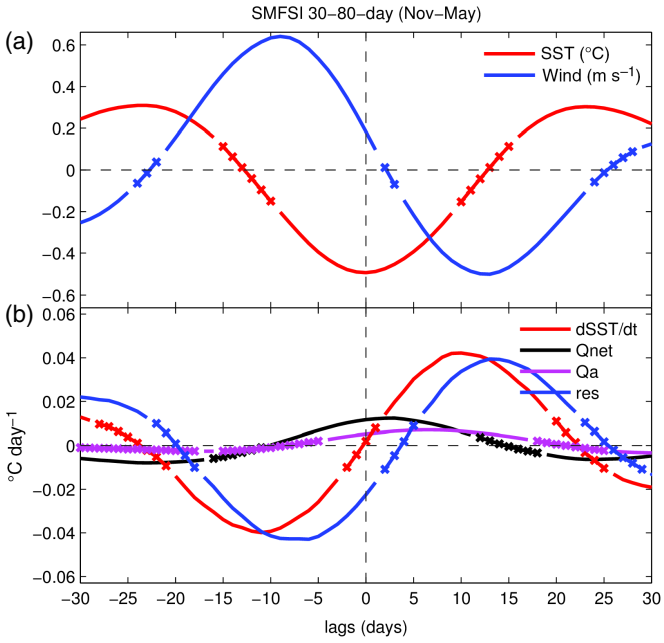

Figure 13. Same as Figure 4, but for the SMFSI: all time series have been band-pass filtered between 30 and 80 days, and only months from November to May are selected.

coming from the continent (Figure 15). SSTAs appear thereafter to damp this coastal wind jet, through a reduced surface heat loss (Figure 16). However, this heat flux feedback is not strong enough to significantly influence surface wind.

6. Summary and discussion

This article investigates the main atmospheric and oceanic causes and consequences of SST ISV over regions of the tropical Atlantic that exhibit the largest variance in intraseasonal SSTAs. We focus on these regions to maximize chances of finding any active air–sea coupling. The largest SST ISV is found over the three main upwelling system fronts, where the climatological SST gradients are the strongest. Two relative maxima are detected in the northern front of the eastern equatorial upwelling (east and west of 10°W, in agreement with previous studies), one off the Angola-Namibia coast and two in the Senegal-Mauritania front (which is investigated here for the first time).

In the equatorial upwelling region, the western SST index exhibits significant variance between 20- and 60-day periods in June–July, with no significant peak in the corresponding wind index. SSTAs are induced by TIW dynamics, and follow a clear eastward propagating pattern, with weaker (stronger) local surface wind over colder (warmer) water, causing anomalous divergence (convergence) to their northwestern sides. The wind response is then mainly accomplished through the SW mechanism as already described by Caltabiano *et al.* (2005). However, the LN mechanism also appears to be active, since anomalous surface wind divergence (convergence) appears sometimes (e.g. Figure 3, lag 0, 15°W) centred over significant positive (negative) SLP anomalies (O'Neil *et al.*, 2010). Further east, the eastern SST and wind indices present synchronous and significant peaks in the 10–20-day range in May–June–July with signature of a regional negative feedback (as in de Coëtlogon *et al.*, 2010).

For both regimes, the SSTAs are mainly controlled by horizontal advection and vertical oceanic mixing. Given these similarities and their geographical proximity, the difference in dominant ISV time-scales appears very surprising. Jouanno *et al.* (2013) have found west of 10°W mainly characterized by free-propagating Yanai (mixed Rossby/gravity) waves (leading to the TIWs as discussed previously), whereas east of 10°W they have found very fast eastward Kelvin waves forced by the surface wind fluctuations. The difference could therefore be due to the mixed-layer depth, which is shallower east of 10°W making this region favourable to Kelvin waves rather than Yanai waves, and increasing then the air–sea coupling at quasi-biweekly time-scales there (de Coëtlogon *et al.*, 2010, 2014).

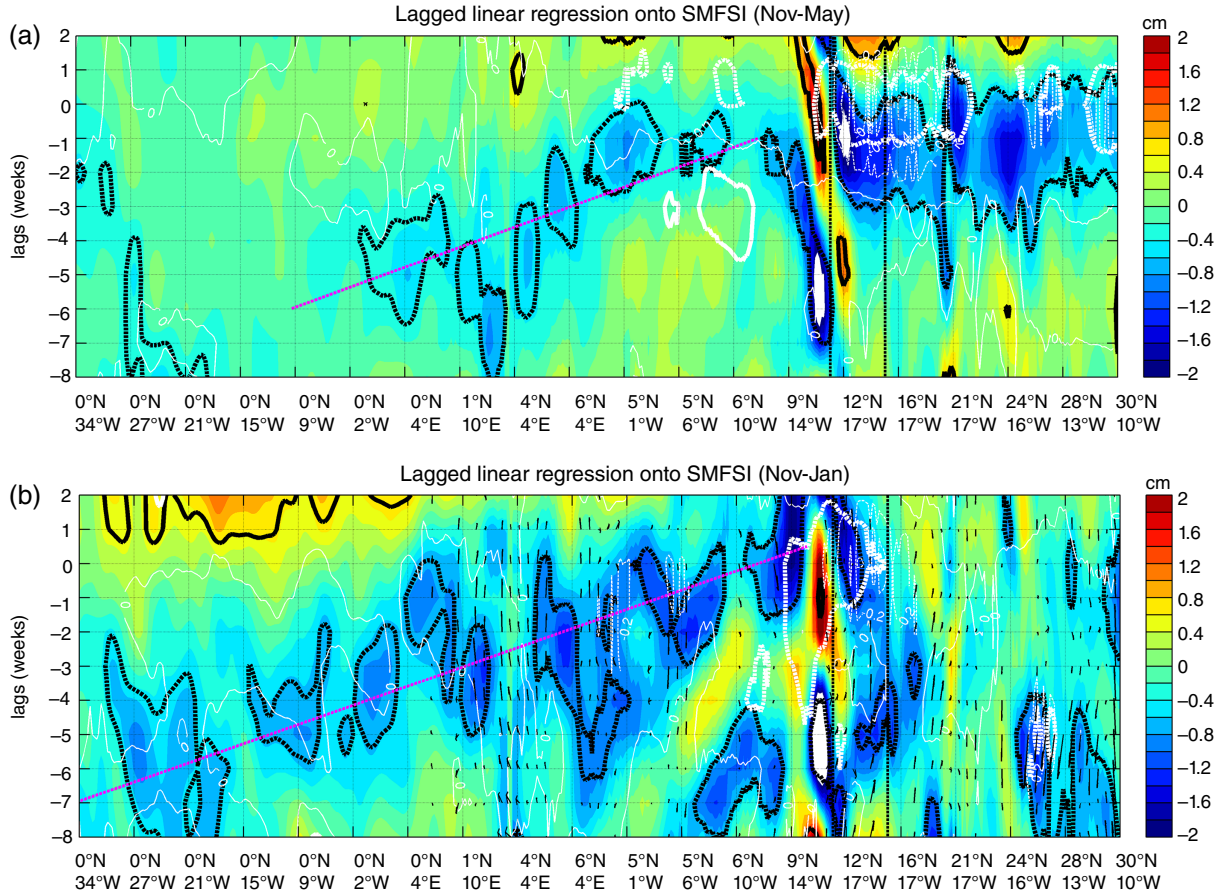

Figure 14. Same as Figure 10, but for the tracking along the Equator (eastward) and the African coast (northward), and regressions are done onto SMFSI. Only months from November to May are selected in (a), and from November to January in (b).

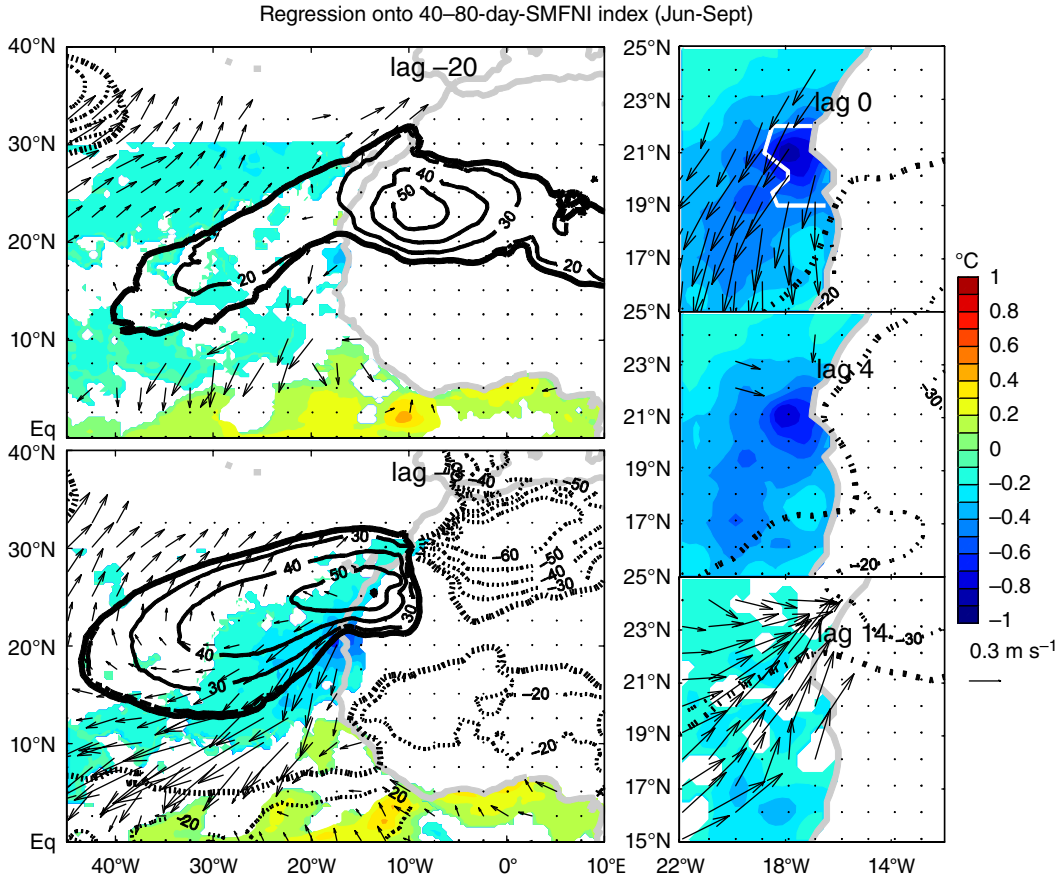

Figure 15. Same as Figure 8, but for the SMFNI: all time series have been band-pass filtered between 40 and 80 days, and only months from June to September are selected.

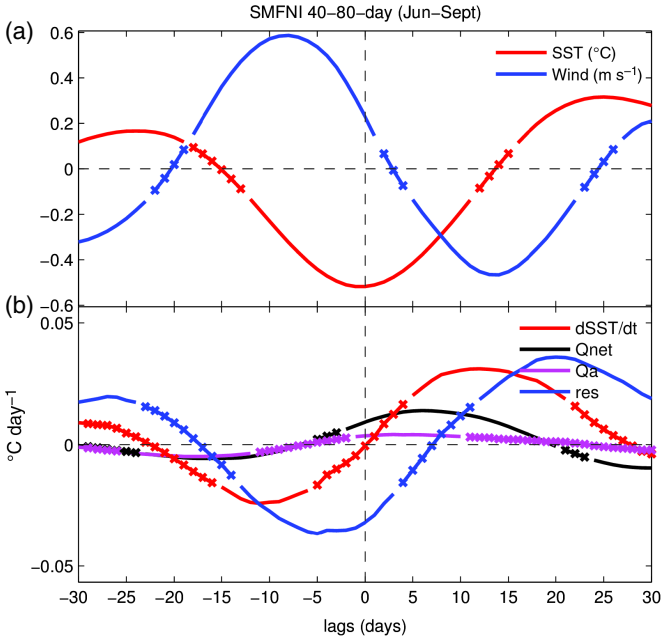

Figure 16. Same as Figure 4, but for the SMFNI: all time series have been band-pass filtered between 40 and 80 days, and only months from June to September are selected.

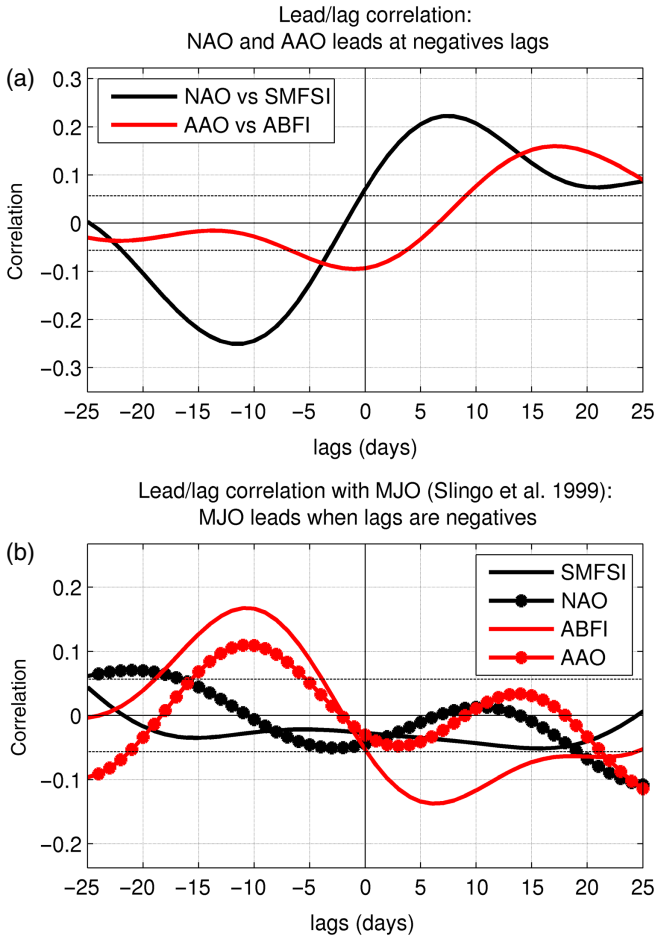

Figure 17. Lagged cross-correlation between (a) NAO and SMFSI indices (black) and AAO and ABFI indices (red); (b) MJO index (Slingo *et al.*, 1999) and SMFSI (black plain line), NAO (black crossed line), ABFI (red plain line), and AAO (red crossed line) indices. Dashed lines represent the 90% confidence level. All time series have been band-pass filtered between 30 and 80 days, and only months from November to May are selected for NAO vs. SMFSI (in (a)), MJO vs. SMFSI and MJO vs. NAO (in (b)); and months from December to June for the others.

Along the Angola-Namibia coast, only one region of strong SST ISV is found around 16–18°S, in the ABF front. Wavelet analysis reveals antagonistic seasonal cycles of SST and wind variance. The SST ISV is found to be maximum from December to June (in the 30–80-day period range), and from June to October (with a peak around 10 days) for the wind. As the vertical stratification of upper oceanic levels is strongest in December–June, local wind fluctuations (even weak) create large SSTAs (Goubanova *et al.*, 2013). Coastal southeasterlies connected to St Helena, AAO as well as the MJO ISV are shown to be the main drivers of the coastal SST cooling. The latter lasts about 25 days, mainly through enhancement of vertical mixing and diffusion. Note that in addition to the local wind forcing, the second barotropic mode of EKW may also impact the cold SSTAs.

Furthermore, SSTAs appear damped by the reduction of latent surface heat flux, and the decrease in oceanic vertical mixing that follows the weakening of southeasterlies (after lag 5). The wind anomalies are found to spatially coincide with the SST minimum, but more than 2 weeks later, therefore excluding an adjustment of the atmospheric boundary layer through the SW mechanism. In addition, no signal is found in the SLP gradients, which implies that the feedback of the SST on the large-scale atmospheric flow in this region could not be detected in our study.

The ABF therefore can be seen as a place where three large-scale atmospheric regimes interact: the MJO, the AAO (partly controlled by the MJO) and the St Helena anticyclone, leading to maximally variant wind fluctuations in the ABF region, with a persistence of more than 1 week. Then, strong stratification associated with outcropping isotherms and with the shallow mixed layer enhances the large upwelling heat flux and surface flux effect.

Off West Africa, the SST ISV is characterized by two regions of strong variance, north and south of 14°N. The southern region (Canaries Upwelling) is most active between November and May, and the northern one between June and September. Two main periodicity ranges are found.

Firstly, a 30–80-day periodicity, more active over the southern front during November–May, and within which coastal SSTAs are mainly created by an anomalous coastal wind jet that derives from fluctuations of the large-scale atmospheric circulation in the North Atlantic. As in the Angola-Namibia region, the surface heat budget reveals that the SST is mostly controlled by wind-driven vertical mixing. Stronger winds cool down the local SST through enhanced vertical mixing in the coastal upwelling. SSTAs are in turn damped mainly by the latent heat flux when it is the coldest, and by the decreased vertical mixing when the wind has become weaker than normal (after lag 3). Horizontal advection, weak but significant, also seems to damp the SSTAs, in agreement with a decrease of the southward surface-water advection from further north (where the SST is colder on average), following a decrease of the surface wind speed. As in the Angola-Namibia region, the local surface wind appears to be impacted by the upwelling SSTAs. However, any significant signal is found in SLP gradients, which suggests a lack of influence on the atmospheric circulation at larger scale. On the other hand, the geostrophic velocity in the heat budget shows that EKWs could also contribute to the SSTA. However, the wave opposes the wind-driven advection effect, and weakly sustains the cold SSTA, instead of damping it. The wave tracking in November–March exhibits clear wave propagation up to 14°N, with a significant SSTA trapped between 8 and 14°N without any consistent significant wind anomaly to explain it.

The second range is a 40–80-day one. It is active in the northern front in June–September. The corresponding SSTAs mainly derive from coastal forcing of the wind associated with a westward-propagating anticyclonic atmospheric pattern coming from the African continent along 26°N, with a speed phase around 0.3 m s^{-1}. Once they reach the coast, northeasterly wind anomalies become a coastal jet that cools down the coastal SST by enhancing vertical mixing in the upwelling. Then, as in the Angola-Namibia and southern Canaries upwelling regions (previously discussed), the cold SSTAs are damped by the reduced latent heat flux and vertical mixing once the wind has become weaker than normal. There again, this feedback does not appear to significantly impact the local surface wind.

A key result from this study is the following. Of the three main upwelling regions in the tropical Atlantic, only the equatorial one appears to be robustly coupled with surface wind. A potential feedback of SST on surface heat fluxes is detected in the Senegal-Mauritania upwelling (southern index, or SMFSI), but weak and in a small area. The surface wind response must then be investigated at a smaller spatial scale there. On the other hand, it is also quite surprising not to find any clear sign of a Madden–Julian Oscillation in SST ISV along the West African coast, as it has been previously found to be a major component of the tropical influence on the North Atlantic circulation (Cassou, 2008). However, the SST influence is only investigated in regions showing an ISV maximum, thus it could be found outside of the upwelling regions.

Acknowledgements

Research leading to these results has been supported by PDI-MSC (an IRD (Institut de Recherche pour le Développement) and UPMC (Université Pierre et Marie Curie) joint programme), the International Joint Laboratory LMI ECLAIRS, and the EU FP7/2007–2013 under grant agreement no. 603521. The SSH dataset has been provided by TOPEX/AVISO. Important suggestions have been made by Mathieu Rouault. Thanks also to the two anonymous reviewers and to Alessendra Giannini whose comments have helped to improve this article.

References

Athié G, Marin F. 2008. Cross-equatorial structure and temporal modulation of intraseasonal variability at the surface of the tropical Atlantic Ocean. *J. Geophys. Res.* **113**: C08020, doi: 10.1029/2007JC004332.

Athié G, Marin F, Treguier AM, Bourlès B, Guiavarc'h B. 2009. Sensitivity of near-surface tropical instability waves to submonthly wind forcing in the tropical Atlantic. *Ocean Modell.* **30**: 241–255.

Bunge L, Provost C, Lilly J, D'Orgeville M, Kartavtseff A, Melice JL. 2006. Variability of the horizontal velocity structure in the upper 1600 m of the water column on the Equator at 10°W. *J. Phys. Oceanogr.* **36**: 1287–1304.

Bunge L, Provost C, Kartavtseff A. 2007. Variability in horizontal current velocities in the central and eastern equatorial Atlantic in 2002. *J. Geophys. Res.* **112**: C02014, doi: 10.1029/2006JC003704.

Caltabiano ACV, Robinson IS, Pezzi LP. 2005. Multi-year satellite observations of instability waves in the tropical Atlantic Ocean. *Ocean Sci. Discuss.* **2**: 1–35.

Caniaux G, Giordani H, Redelsperger JL, Guichard F, Key E, Wade M. 2011. Couplings between the Atlantic cold tongue and the African monsoon in boreal spring and summer. *J. Geophys. Res.* **116**: C04003, doi: 10.1029/2010JC006570.

Cassou C. 2008. Intraseasonal interaction between the Madden–Julian Oscillation and the North Atlantic Oscillation. *Nature* **445**: 523–527, doi: 10.1038/nature07286.

Chauvin F, Roehrig R, Lafore JP. 2010. Intraseasonal variability of the Saharan heat low and its link with midlatitudes. *J. Clim.* **23**: 2544–2561.

Chelton DB, Xie SP. 2010. Coupled ocean–atmosphere interaction at oceanic mesoscales. *Oceanography* **23**: 52–69, doi: 10.5670/oceanog.2010.05.

Chelton DB, Esbensen SK, Schlax MG, Thum N, Freilich MH, Wentz FJ, Gentemann CL, McPhaden MJ, Schopf FJ. 2001. Observations of coupling between surface wind stress and sea surface temperature in the eastern tropical Pacific. *J. Clim.* **14**: 1479–1498.

Chelton DB, Schlax MG, Freilich MH, Milliff RF. 2004. Satellite measurements reveal persistent small-scale features in ocean winds. *Science* **303**: 978–983.

Chelton DB, Freilich MF. 2005. Scatterometer-based assessment of 10-m wind analyses from the operational ECMWF and NCEP numerical weather prediction models. *Mon. Weather Rev.* **133**: 409–429, doi: 10.1175/MWR-2861.1.

de Coëtlogon G, Janicot S, Lazar A. 2010. Intraseasonal variability of the ocean–atmosphere coupling in the Gulf of Guinea during boreal spring and summer. *Q. J. R. Meteorol. Soc.* **136**: 426–441.

de Coëtlogon G, Leduc-Leballeur M, Meynadier R, Bastin S, Diakhaté M, Eymard L, Giordani H, Janicot S, Lazar A. 2014. Atmospheric response to sea-surface temperature in the eastern equatorial Atlantic at quasi-biweekly time-scales. *Q. J. R. Meteorol. Soc.* **140**: 1700–1714, doi: 10.1002/qj.2250.

Davey MK, Huddleston M, Sperber KR, Braconnot P, Bryan F, Chen D, Colman RA, Cooper C, Cubasch U, Delecluse P, DeWitt D, Fairhead L, Flato G, Gordon C, Hogan T, Ji M, Kimoto M, Kitoh A, Knutson TR, Latif M, Le Treut H, Li T, Manabe S, Mechoso CR, Meehl GA, Power SB, Roeckner E, Terray L, Vintzileos A, Voss R, Wang B, Washington WM, Yoshikawa I, Yu JY, Yukimoto S, Zebiak SE. 2002. STOIC: A study of coupled model climatology and variability in tropical ocean regions. *Clim. Dyn.* **18**: 403–420.

Demarcq H, Faure V. 2000. Coastal upwelling and associated retention indices derived from satellite SST. Application to *Octopus vulgaris* recruitment. *Oceanolog. Acta* **23**: 391–408.

Dieng AL, Eymard L, Sall SM, Lazar A, Leduc-Leballeur M. 2014. Analysis of strengthening and dissipating mesoscale convective systems propagating off the West African coast. *Mon. Weather Rev.* **142**: 4600–4623.

Ding H, Keenlyside NS, Latif M. 2009. Seasonal cycle in the upper equatorial Atlantic Ocean. *J. Geophys. Res.* **114**: C09016, doi: 10.1029/2009JC005418.

Doi T, Tozuka T, Sasaki H, Masumoto Y, Yamagata T. 2007. Seasonal and interannual variations of oceanic conditions in the Angola Dome. *J. Phys. Oceanogr.* **37**: 2698–2713.

Düing W, Hisard P, Katz E, Meincke J, Miller L, Moroshkin KV, Philander G, Ribnikov AA, Voit K, Weisberg R. 1975. Meanders and long waves in equatorial Atlantic. *Nature* **257**: 280–284.

Flament PJ, Kennan SC, Knox RA, Niiler PP, Bernstein RL. 1996. The three-dimensional structure of an upper ocean vortex in the tropical Pacific Ocean. *Nature* **383**: 610–613.

Foltz GR, McPhaden MJ. 2004. The 30–70 day oscillations in the tropical Atlantic. *Geophys. Res. Lett.* **31**: L15205, doi: 10.1029/2004GL020023.

Foltz GR, Schmid C, Lumpkin R. 2013. Seasonal cycle of the mixed layer heat budget in the northeastern tropical Atlantic Ocean. *J. Clim.* **26**: 8169–8188.

Giordani H, Voldoire A, Caniaux G. 2013. Intraseasonal mixed-layer heat budget in the equatorial Atlantic during the cold tongue development in 2006. *J. Geophys. Res. Oceans* **118**: 650–671, doi: 10.1029/2012JC008280.

Goubanova K, Illig S, Machu E, Garçon V, Dewitte B. 2013. SST subseasonal variability in the central Benguela upwelling system as inferred from satellite observations (1999–2009). *J. Geophys. Res. Oceans* **118**: 4092–4110, doi: 10.1002/jgrc.20287.

Gu G, Adler RF. 2004. Seasonal evolution and variability associated with the West African monsoon system. *J. Clim.* **17**: 3364–3377.

Hayes SP, McPhaden MJ, Wallace JM. 1989. The influence of sea surface temperature on surface wind in the eastern equatorial Pacific: Weekly to monthly variability. *J. Clim.* **2**: 1500–1506.

Hermes JC, Reason CJC. 2009. Variability in sea-surface temperature and winds in the tropical south-east Atlantic Ocean and regional rainfall relationship. *Int. J. Climatol.* **29**: 11–21.

Huang Y, Ramaswamy V, Soden B. 2007. An investigation of the sensitivity of the clear-sky outgoing longwave radiation to atmospheric temperature and water vapor. *J. Geophys. Res.* **112**: D05104, doi: 10.1029/2005JD006906.

Jochum M, Murtugudde R, Ferrari R, Malanotte-Rizzoli P. 2005. The impact of horizontal resolution on the tropical heat budget in an Atlantic Ocean model. *J. Clim.* **18**: 841–851.

Jouanno J, Marin F, du Penhoat Y, Sheinbaum J, Molines JM. 2011. Seasonal heat balance in the upper 100 m of the equatorial Atlantic Ocean. *J. Geophys. Res.* **116**: C09003, doi: 10.1029/2010JC006912.

Jouanno J, Marin F, du Penhoat Y, Molines JM. 2013. Intraseasonal modulation of the surface cooling in the Gulf of Guinea. *J. Phys. Oceanogr.* **43**: 382–401, doi: 10.1175/JPO-D-12-053.1.

Kennan SC, Flament PJ. 2000. Observations of a tropical instability vortex. *J. Phys. Oceanogr.* **30**: 2277–2301.

Leduc-Leballeur M, de Cöetlogon G, Eymard L. 2013. Air–sea interaction in the Gulf of Guinea at intraseasonal time-scales: Wind bursts and coastal precipitation in boreal spring. *Q. J. R. Meteorol. Soc.* **139**: 387–400, doi: 10.1002/qj.1981.

Lindzen RS, Nigam S. 1987. On the role of sea surface temperature gradients in forcing low level winds and convergence in the Tropics. *J. Atmos. Sci.* **44**: 2418–2436.

Liu WT, Xie X, Polito PS, Xie S-P, Hashizume H. 2000. Atmospheric manifestation of tropical instability wave observed by QuikSCAT and Tropical Rainfall Measuring Mission. *Geophys. Res. Lett.* **27**: 2545–2548, doi: 10.1029/2000GL011545.

Madden RA, Julian PR. 1971. Detection of a 40–50 day oscillation in the zonal wind in the tropical Pacific. *J. Atmos. Sci.* **28**: 702–708.

Marchesiello P, Estrade P. 2010. Upwelling limitation by onshore geostrophic flow. *J. Mar. Res.* **68**: 37–62.

Okumura Y, Xie S-P. 2006. Some overlooked features of tropical Atlantic climate leading to a new Niño-like phenomenon. *J. Clim.* **19**: 5859–5874.

O'Neill LW, Esbensen SK, Thum N, Samelson R, Chelton DB. 2010a. Dynamical analysis of the boundary layer and surface wind responses to mesoscale SST perturbations. *J. Clim.* **23**: 559–581.

O'Neill LW, Chelton DB, Esbensen SK. 2010b. The effects of SST-induced surface wind speed and direction gradients on midlatitude surface vorticity and divergence. *J. Clim.* **23**: 255–281.

Peter AC, Le H'enaff M, du Penhoat Y, Menkes CE, Marin F, Vialard J, Caniaux G, Lazar A. 2006. A model study of the seasonal mixed layer heat budget in the equatorial Atlantic. *J. Geophys. Res.* **111**: C06014, doi:10.1029/2005JC003157.

Pohl B, Fauchereau N. 2012. The southern annular mode seen through weather regimes. *J. Clim.* **25**: 3336–3354.

Polo I, Lazar A, Rodriguez-Fonseca B, Arnault S. 2008. Oceanic Kelvin waves and tropical Atlantic intraseasonal variability: 1. Kelvin wave characterization. *J. Geophys. Res.* **113**: C07009, doi: 10.1029/2007JC004495.

Qiao L, Weisberg RH. 1995. Tropical instability wave kinematics: Observations from the Tropical Instability Wave Experiment. *J. Geophys. Res.* **100**: 8677–8693, doi: 10.1029/95JC00305.

Reynolds RW, Smith TM, Liu C, Chelton DB, Caset KS, Schlax MG. 2007. Daily high-resolution blended analyses for sea surface temperature. *J. Clim.* **20**: 5473–5496.

Richter I, Xie SP, Behera S, Doi T, Masumoto Y. 2014. Equatorial Atlantic variability and its relation to mean state biases in CMIP5. *Clim. Dyn.* **42**: 171–188, doi: 10.1007/s00382-012-1624-5.

Roy C. 1989. Fluctuations des vents et variabilité de l'upwelling devant les côtes du Sénégal. *Oceanolog. Acta* **12**: 361–369.

Saha S, Moorthi S, Pan H, Wu X, Wang J, Nadiga S, Tripp P, Kistler R, Woollen J, Behringer D, Liu H, Stokes D, Grumbine R, Gayno G, Wang J, Hou Y, Chuang H, Juang H, Sela J, Iredell M, Treadon R, Kleist D, Van Delst P, Keyser D, Derber J, Ek M, Meng J, Wei H, Yang R, Lord S, van den Dool H, Kumar A, Wang W, Long C, Chelliah M, Xue Y, Huang B, Schemm J, Ebisuzaki W, Lin R, Xie P, Chen M, Zhou S, Higgins W, Zou C, Liu Q, Chen Y, Han Y, Cucurull L, Reynolds R, Rutledge G, Goldberg M. 2010. Supplement to the NCEP climate forecast system reanalysis. *Bull. Am. Meteorol. Soc.* **91**: 1015–1057.

Seo H, Jochum M, Murtugudde R, Miller AJ, Roads JO. 2007. Feedback of tropical instability-wave-induced atmospheric variability onto the ocean. *J. Clim.* **20**: 5842–5855.

Slingo JM, Rowell DP, Sperber KR, Nortley F. 1999. On the predictability of the interannual behaviour of the Madden–Julian Oscillation and its relationship with El Niño. *Q. J. R. Meteorol. Soc.* **125**: 583–609.

Small RJ, deSzoeke SP, Xie S-P, O'Neill L, Seo H, Song Q, Cornillon P, Spall M, Minobe S. 2008. Air–sea interaction over ocean fronts and eddies. *Dyn. Atmos. Oceans* **45**: 274–319.

Sweet W, Fett R, Kerling J, La Violette P. 1981. Air–sea interaction effects in the lower troposphere across the north wall of the Gulf Stream. *Mon. Weather Rev.* **109**: 1042–1052.

Torrence C, Compo GP. 1998. A practical guide to wavelet analysis. *Bull. Am. Meteorol. Soc.* **79**: 61–78.

Wade M, Lazar A, Peter AC. 2015. 'Thermal impact of oceanic Kelvin waves along the west African coast'. *PIRATA-PREFACE-CLIVAR Tropical Atlantic Variabily Confrence*, 24–27 August 2015, Cape Town, South Africa.

Wai MMK, Stage SA. 1989. Dynamical analyses of marine atmospheric boundary layer structure near the Gulf Stream oceanic front. *Q. J. R. Meteorol. Soc.* **115**: 29–44.

Wainer I, Clauzet G, Servain J, Soares J. 2003. Time scales of upper ocean temperature variability inferred from the PIRATA data (1997–2000). *Geophys. Res. Lett.* **30**: 8004, doi: 10.1029/2002GL015147.

Wallace JM, Mitchell TP, Deser C. 1989. The influence of sea-surface temperature on surface wind in the eastern equatorial Pacific: Seasonal and interannual variability. *J. Clim.* **2**: 1492–1499.

Xie S-P. 2004. Satellite observations of cool ocean–atmosphere interaction. *Bull. Am. Meteorol. Soc.* **85**: 195–208.

Xie S-P, Carton JA. 2004. Tropical Atlantic variability: Patterns, mechanisms, and impacts. In *Earth Climate: The Ocean–Atmosphere Interaction*, Wang C, Xie S-P, Carton JA. (eds.) *Geophysical Monograph* **147**: . 121–142 AGU: Washington, DC.

Yamagata T, Iizuka S. 1995. Simulation of the tropical thermal domes in the Atlantic: A seasonal cycle. *J. Phys. Oceanogr.* **25**: 2129–2140.

